Importance of thermochemical pressurization in the dynamic weakening of the Longmenshan Fault during the 2008 Wenchuan earthquake: Inferences from experiments and modeling

Jianye Chen,[1,2] Xiaosong Yang,[1] Qingbao Duan,[1] Toshi Shimamoto,[1] and Christopher J. Spiers[2]

[1]   We determined the internal structure and mineral composition of the Yingxiu-Beichuan fault zone at the Zhaojiagou exposure and measured frictional and transport properties of the fault rocks collected to gain a better understanding of dynamic weakening mechanisms during seismic fault motion. This fault is a major fault in the Longmenshan fault system that caused the 2008 Wenchuan earthquake. The exposure studied is located midway along the surface rupture, close to where the largest coseismic displacement occurred. High-velocity friction experiments reveal exponential slip weakening from a peak friction toward a steady state value. Slip weakening is more pronounced for water-dampened gouge than dry gouge, suggesting thermal pressurization. The fault gouge has a very low permeability ($< 10^{-21}\,\mathrm{m}^2$ at 165 MPa effective pressure) and is surrounded by fault breccia with a permeability of 10^{-19} to $10^{-17}\,\mathrm{m}^2$, grading into less permeable, fractured country rocks. The fault zone thus exhibits a "conduit/barrier" structure, allowing fluid flow only in the breccia zone. We numerically modeled coseismic slip weakening including thermal pressurization and mineral dehydration/decarbonation, basing our calculation on measured frictional and transport properties and on the slip history inferred for the Wenchuan earthquake. The results indicate that (1) thermochemical pressurization played an important role in causing dynamic slip weakening, (2) the slip-weakening distance is similar to the seismologically determined values, and (3) pore pressures might have exceeded the normal stress, thus maintaining temperatures below 600°C. Interestingly, enough heat was generated to fully remove and thermally pressurize the interlayer water from smectite, contributing an excess pore pressure of ~ 6 MPa. In addition, we found that the incorporation of state-dependent fluid properties predicts much more efficient fluid pressurization than using constant properties. The dramatic weakening predicted probably offers a compelling explanation for the large coseismic displacement and slip acceleration observed near Beichuan city.

1. Introduction

[2]   The catastrophic Wenchuan earthquake (M_s 8.0) struck Sichuan, China on 12 May 2008. Coseismic surface rupture occurred over a distance of 240 km along the northeast striking Longmenshan fault zone (LFZ), with a maximum vertical offset of ~ 9 m [*Xu et al.*, 2009; *Zhang et al.*, 2010]. A maximum displacement of ~ 7.3 m and a corresponding slip rate of 1.25 m/s were inferred from seismological inversion [*Zhang et al.*, 2009]. This also yielded an average stress drop of 18 MPa, which double that characteristic of a typical continental interior earthquake [*Kanamori*, 1994]. The Wenchuan earthquake is the first with such a large magnitude recorded on a high-angle reverse fault within a continental interior [*Zhang et al.*, 2010]. Besides high tectonically generated deviatoric stress, a high pore pressure at depth may be required for a reverse fault to yield a mega-earthquake [*Sibson et al.*, 1988]. Such pore pressures are only possible if the fault zone is impermeable enough to seal high-pressure fluid within the fault zone [*Faulkner and Rutter*, 2000]. A slip-weakening mechanism may also be required to account for the large coseismic displacement observed, which was much higher

[1]State Key Laboratory of Earthquake Dynamics, Institute of Geology, China Earthquake Administration, Beijing, China.

[2]HPT Laboratory, Department of Earth Sciences, Utrecht University, Utrecht, Netherlands.

Corresponding author: J. Chen, State Key Laboratory of Earthquake Dynamics, Institute of Geology, China Earthquake Administration, Qijiahuozi, Dewai Area, Chaoyang District, Beijing 100029, China. (jychen@ies.ac.cn)

than experimentally inferred slip-weakening distances at nucleation slip rates [e.g., *Ohnaka and Shen*, 1999].

[3] Theoretical studies have focused on thermal pressurization (TP) as an important slip-weakening mechanism, at both the coseismic slip [*Lachenbruch*, 1980; *Mase and Smith*, 1985; *Rice*, 2006] and rupture nucleation [*Segall and Rice*, 2006; *de Lorenzo and Lpddo*, 2010] of an earthquake. Other high-velocity slip-weakening mechanisms include silica gel lubrication [*Di Toro et al.*, 2004], bulk melting [*Tsutsumi and Shimamoto*, 1997; *Hirose and Shimamoto*, 2005], flash heating [*Rice*, 1999], and nanoparticle lubrication [*Han et al.*, 2010; *Reches and Lockner*, 2010]. The principle of TP is that the pressure of pore fluid, trapped inside a slipping fault, builds up due to frictional heating, thus reducing the effective normal stress acting on the fault plane and hence the shearing resistance of the fault [*Lachenbruch*, 1980; *Mase and Smith*, 1985]. TP can cause additional effects such as increased slip distance [*Rice*, 2006] and an increase in rupture velocity [*Bizzarri and Cocco*, 2006].

[4] A growing body of natural and experimental evidence has recently shown that reactions induced by frictional heating may also be more important than previously realized in producing weakening effects during fault motion [*Hirono et al.*, 2006, 2008; *Han et al.*, 2007; *Hirose and Bystricky*, 2007; *Brantut et al.*, 2008; *Hamada et al.*, 2009; *Ferri et al.*, 2010; *Yamaguchi et al.*, 2011]. Aside from the production of minerals that could make faults much weaker than expected from the static mineral assemblage [*Vrolijk and van der Pluijm*, 1999], dehydration reactions [*Brantut et al.*, 2008; *Famin et al.*, 2008; *Ferri et al.*, 2010] may liberate fluid into the pore space, thus building up pore pressure and reducing fault shearing resistance. On the other hand, some reactions have a strong endothermic effect that can inhibit temperature rise and hence reduce TP effects [*Brantut et al.*, 2011]. Few experiments have yet been successful in verifying the coseismic TP process [*Sulem et al.*, 2007; *Ujiie et al.*, 2011], not to mention the influence of chemical reactions upon it. However, numerical modeling has demonstrated that the process is possible [e.g., *Wibberley and Shimamoto*, 2005; *Noda and Shimamoto*, 2005; *Bizzarri and Cocco*, 2006; *Mizoguchi and Shimamoto*, 2008]. Recent modeling using laboratory-derived physical properties is now leading to refinement of TP modeling efforts [*Wibberley and Shimamoto*, 2005; *Tanikawa et al.*, 2009] and to improved understanding of the coseismic thermochemical pressurization combing TP and the effect of fluid release due to mineral decomposition [*Brantut et al.*, 2010; *Sulem and Famin*, 2009], and of their effect on rupture propagation.

[5] With those development in understanding of the seismic fault motion, this paper reports mineralogical composition and in situ frictional and transport properties of fault rocks collected from an exposure on the Yingxiu-Beichuan fault, the major coseismic fault in the LFZ that caused the 2008 Wenchuan earthquake. With the lab-constrained fault rock properties, we then numerically model coseismic slip inside a fluid-saturated fault zone including thermochemical pressurization. We performed parametric analysis with respect to a reference case with measured properties to quantify the impacts of different variables on the weakening processes. The results show that the thermochemical

processes are likely to control the slip weakening during the Wenchuan earthquake. Our results will be useful in future realistic modeling of the dynamic rupture propagation during the Wenchuan earthquake, thereby in testing how much we understand the origin of the large displacement and slip acceleration behavior observed near our sampling site.

2. Geological Setting and Fault Exposure

[6] The Longmenshan fault system constitutes three parallel subfaults, Wenchuan-Maoxian, Yingxiu-Beichuan, and Guanxian-Jiangyou faults from northwest to southeast (Figure 1a). The Wenchuan earthquake activated motion on two of them, with the coseismic surface rupture being denoted by thick black lines. The segment from Gaochuan to Beichuan is shifted eastward by ~ 3 km from the general northeast striking trend of the Yingxiu-Beichuan fault. An enlarged map near Beichuan (Figure 1b) shows that the surface rupture trace exhibits a transition from cutting into the Cambrian block to propagating northeast along stratum boundaries. Note that the largest coseismic offset of the Wenchuan earthquake occurred near Beichuan (Figure 1c) and that the surface rupture along the fault showed an abrupt jump there, from a vertical offset of 1.7 to 8.6 m and from a horizontal offset of 1.6 to 2.5 m, respectively [*Zhang et al.*, 2010]. As shown in Figure 1d, the slip rates at various depths exhibited an abrupt acceleration as the rupture approached Beichuan city, and acceleration is also inferred as the rupture propagated from depth upward [*Zhang et al.*, 2009]. The fault motion near Beichuan was completed in two stages. One slip event occurs between 36 and 41 s (referred to as "pre-slip"), and the other is the main slip, occurring between 48 and 58 s (Figure 1e).

[7] In this study, the Zhaojiagou (ZJG) exposure, located at ~ 3 km southwest of Beichuan city, was systematically investigated. Located in a cliff (Figure 2a), the ZJG exposure is well exposed. The fault here strikes at an azimuth of 45° and dips 64°–78° to the NW (Figure 2b). The principal slip surface cuts through the carbonate-rich layer. The fault gouge is either black or gray in color and could be distinguishable easily from the amount of visible clasts of less than 30%, following the classification of *Sibson* [1977]. Surrounding fault breccias were characterized by an increase in the amount of visible clasts and by the development of fractures (Figures 2c and 2d). The fault zone at this exposure consists of different units. From west to east, they were (1) fractured limestone, (2) cemented coarse breccias, (3) coarse breccias, (4) weakly foliated fine breccias, (5) gray and black fault gouges, (6) weakly foliated fine breccias, (7) coarse breccias, and (8) fractured sandstone.

[8] The fault core [*Caine et al.,* 1996] is extremely narrow (~ 20 cm), consisting of gray gouge in the center and surrounding weakly foliated yellowish fault breccias (Figures 2c and 2d). The thickness of the gray gouge ranges from 10 to 31 mm, with a mean of 20 mm and standard deviation of 7.2 mm (15 measurements at an interval of ~ 10 cm). It is interesting that there developed a thin black gouge layer (< 7 mm) adjacent to the gray gouge (Figures 2c and 2d). These gouges consisted of a very fine, tacky, clay-rich material exhibiting ductile behavior when wet. They often branch to the adjacent breccia zone. Figure 2e is a
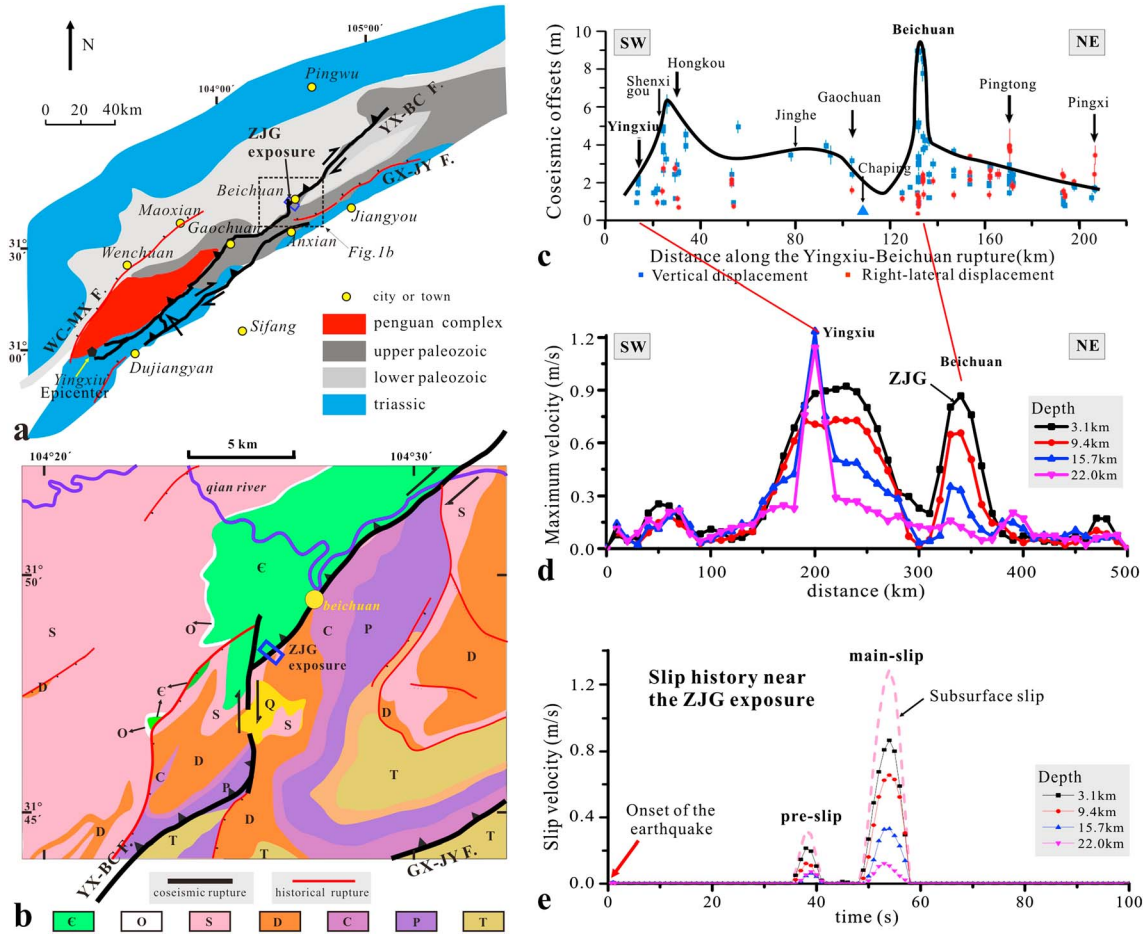
Figure 1. Geological setting and slip history of the Wenchuan earthquake. (a) Location of the study area and regional geological map of the Longmenshan fault system, consisting of three fault zones, the Wenchuan-Maoxian Fault (WC-MX F.), Yingxiu-Beichuan Fault (YX-BC F.), and Guanxian-Jiangyou Fault (GX-JY F.). (b) Enlarged geological map near the study area. (c) Coseismic slip distributions of surface rupture along the Yingxiu-Beichuan Fault, revised after *Zhang et al.* [2010] by adding a new data point for Chaping [*Hou et al.*, 2012] and an interpretive envelope curve. (d) Maximum slip velocities at various depths along the Yingxiu-Beichuan Fault during the Wenchuan earthquake. (e) Slip history at a location near the exposure studied at various depths. Notations of symbols for stratum in Figure 1b are Є for Cambrian; O, Ordovician; S, Silurian; D, Devonian; C, Carboniferous; P, Permian; T, Triassic. The data in Figures 1d and 1e are from the inversion results given by *Zhang et al.* [2009]. The slip history presented in Figure 1e is 3.8 km northeast of the exposure studied. To obtain subsurface slip history, we extrapolated the slip history data for 3.1 km depth, derived from the geophysical inversion by *Zhang et al.* [2009], constraining the total displacement to be equal to that measured at the surface by geological survey (Figure 1c).

photomicrograph under crossed polarized light, showing a slice of specimen (~ 14 mm thick) composed of fault gouge and fault breccia. Further microscopic examination on it revealed that the coseismic slip of the Wenchuan earthquake might be localized. The slip may concentrate in part of the width of the gouge zone (~ 4 mm thick, corresponding to the black gouge in Figure 2d) or in an even more localized band (< 1 mm thick, at the left margin of the gouge zone in Figure 2e). It is difficult to make sure which was the principal slip zone during the Wenchuan earthquake. Considering that the black gouge is not continuous on the exposure, we take the evenly distributed slip as a reference case, and the influence of localization on coseismic slip weakening is discussed in detail in section 5.4.4.

3. Sampling and Experimental Methods

3.1. Sampling

[9] A roughly 50 cm thick surface layer was removed to eliminate weathered rocks. To provide sufficient data on spatial variation of rock properties to model coseismic slip behavior, the fault gouge and adjacent rocks were carefully sampled. Cylindrical samples used for measuring transport properties were taken by inserting thin-walled (0.1 mm thick) copper tubes with an internal diameter of 20 mm into the sexposure and extracting them with the enclosed material. Stainless steel tubes of 22 mm internal diameter were used when the fault rock was too hard to use copper tube. The cores were transferred into polyolefin heat-shrinkable tubes
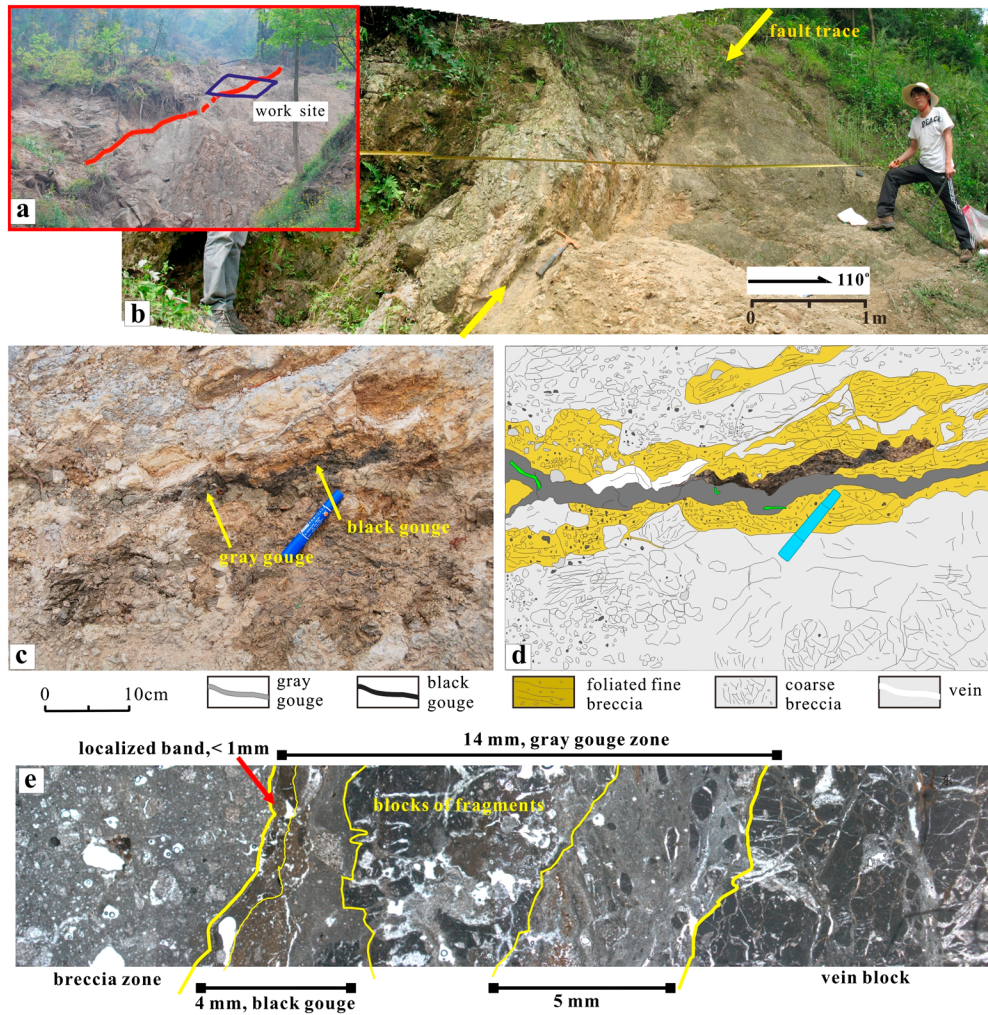
Figure 2. Internal structure of the fault zone. Photographs of the (a, b) ZJG exposure and (c) fault core structure and (d) the interpretive sketch. (e) Microstructure of the slip zone. The GPS location is104°25′57.61″E and 31°48′22.44″N. Note that the exposure is in a cliff, so it is difficult to take a more panoramic view.

and then heat jacketed to protect the cores in cylinder shape. For cohesive rocks like the country rock, hand specimens were collected in the field and coring was done in the laboratory. All the samples were cored parallel to fault surface, except for the gouge sample, which were cored perpendicular to foliation.

### 3.2. Mineralogical Analysis

[10] X-ray diffraction (XRD) was used to determine relative mineral content including semiquantitative analysis for clay minerals. Unoriented, hand-powdered bulk samples were analyzed over a 2θ range of 3° to 45° at a scan rate of 2°/min with a step width of 0.02°, employing a Dmax 12 kW X-ray powder diffractometer and CuK-α radiation. Bulk powder samples gave a first evaluation of the relative amounts of bulk clays; the composition of which was further verified by analyzing the clay-sized portion. After centrifuging, suspensions of < 2 mm particle size were deposited on glass slides and scanned in the diffractometer. Ethylene glycol was used to hydrate the clay samples so as to recognize swelling components (smectite or illite/smectite

mix layer). Heating to 550°C helped distinguish kaolinite from chlorite. The method of semiquantitative analysis of clay minerals followed that of *Lin et al*. [1992].

3.3. High-Velocity Friction Tests

[11] Friction experiments were conducted at seismic slip rate under both "dry" (atmospheric humidity) and wet conditions, on the gray gouge and on simulated gouge prepared from the fault breccia. The samples were prepared by lightly tapping in a mortar to produce powder, sieving to a grain size of less than 125 μm, and then oven drying at 80°C for 48 h, immediately prior to experimentation. Experiments were conducted using the low-to-high velocity, rotary-shear friction apparatus recently installed at the Institute of Geology, China Earthquake Administration, Beijing [*Yao et al*., 2013]. The apparatus is capable of producing slip velocities ranging from tens of mm/year to seismic slip rates of around a few m/s, but we focused on frictional properties at high slip rate (1.3 m/s). The procedures for experimentation followed *Mizoguchi et al*. [2007]. A 1.0 mm thick (2.3 g) powder layer was sandwiched between a pair of
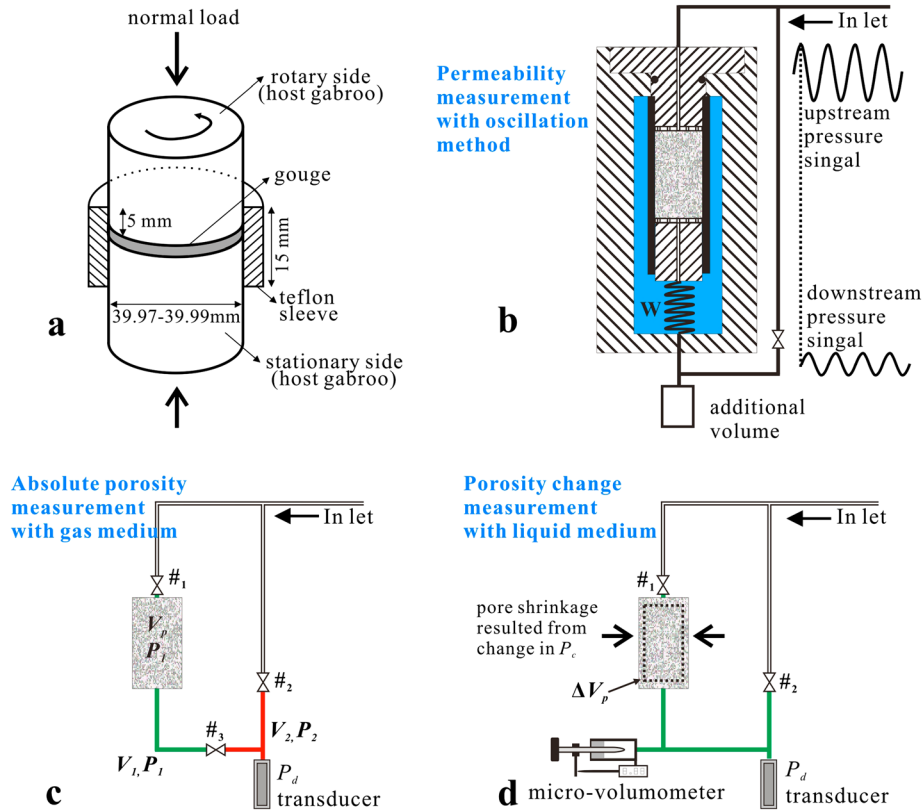
Figure 3. (a) Sample assembly of the high-velocity rotary frictional tests. Diagrams illustrating (b) permeability measurement using the pore pressure oscillation method, (c) absolute porosity measurement with gas medium, and (d) porosity change measurement during each step change in confining pressure.

gabbro cylinders of ~ 40 mm in diameter, of which the outer surfaces had been ground with a diamond grinding wheel #150 (100 μm) using a cylindrical grinder and the end surfaces had been roughened by grinding with #80 silicon carbide powder (180 μm). A Teflon sleeve was mounted on this sample assembly to prevent gouge loss (Figure 3a). An axial force corresponding to the normal stress applied during each experiment was then imposed on the gouge and maintained for ~ 5 min. This is held near constant (within ~ 1%) by employing a Bellofram cylinder filled with compressed air to serve as a buffer. The gouge was then pretreated by sliding at a slow rate (1.3 mm/s) for about 15 s, at which point the slip rate was increased instantly to 1.3 m/s to conduct a high-velocity friction experiment at a constant slip rate. Slip rate was incremented instantaneously by changing the gear assembly from intermediate slip rates to high-velocity line without stopping the servomotor.

[12] For wet experiments, 20 wt % distilled H_2O was added to the gouge layer to fulfill the water-saturated condition using a 0.5 ml syringe. Other procedures were as for dry experiments. The pore fluid resided within the gouge porosity, enclosed by the gabbro (commercial decorative Indian gabbro, permeability $< 10^{-22}$ m^2) and the poorly sealed Teflon sleeve, at an unmeasured pressure (likely between 0.1 and 0.65 MPa according to numerical modeling of the experiments, see section 6.2), determined by competition between thermal pressurization and leakage past the Teflon sleeve. The effects of heating and decomposition of Teflon sleeves have recently been called into question

[Sawai et al., 2012] in high-velocity experiments on gouge samples because released fluorine probably reacts with the gouge near its outer edge. However, we consider this heating/decomposition effect to be negligible in our experiments because the (measured) Teflon friction was very low (Figure 4a) and because our sample assembly had a larger diameter (~ 40 mm) than most previous studies (~ 25 mm), so any effects of Teflon decomposition would be volumetrically insignificant (if decomposition occurred at all). Data on torque, axial force, displacement, revolution rate, and number of revolution were recorded with a digital data recorder with sampling rates of 2000 Hz. Data processing followed Togo et al. [2011].

3.4. Transport Property Measurement

[13] Integrated permeability/porosity measurements were performed using a high-pressure fluid flow apparatus, at room temperature and under confining pressure to 180 MPa, using water as confining medium. In a typical measurement, the rubber-tube jacked cylindrical sample with spacers (double layers of steel mesh, #240 and #30, of 0.6 mm thick in total) at its two ends was inserted inside the vessel, connected to the upstream and downstream reservoirs. Each experiment was initiated by imposing a confining pressure of 10 MPa. The pore fluid system was subsequently evacuated (~ 15 min) and pressurized with nitrogen. The measuring procedure adopted was as follows: (1) determine the absolute porosity of the dry sample at an initial effective pressure of P_{e0} using nitrogen as pore fluid, (2) introduce water into
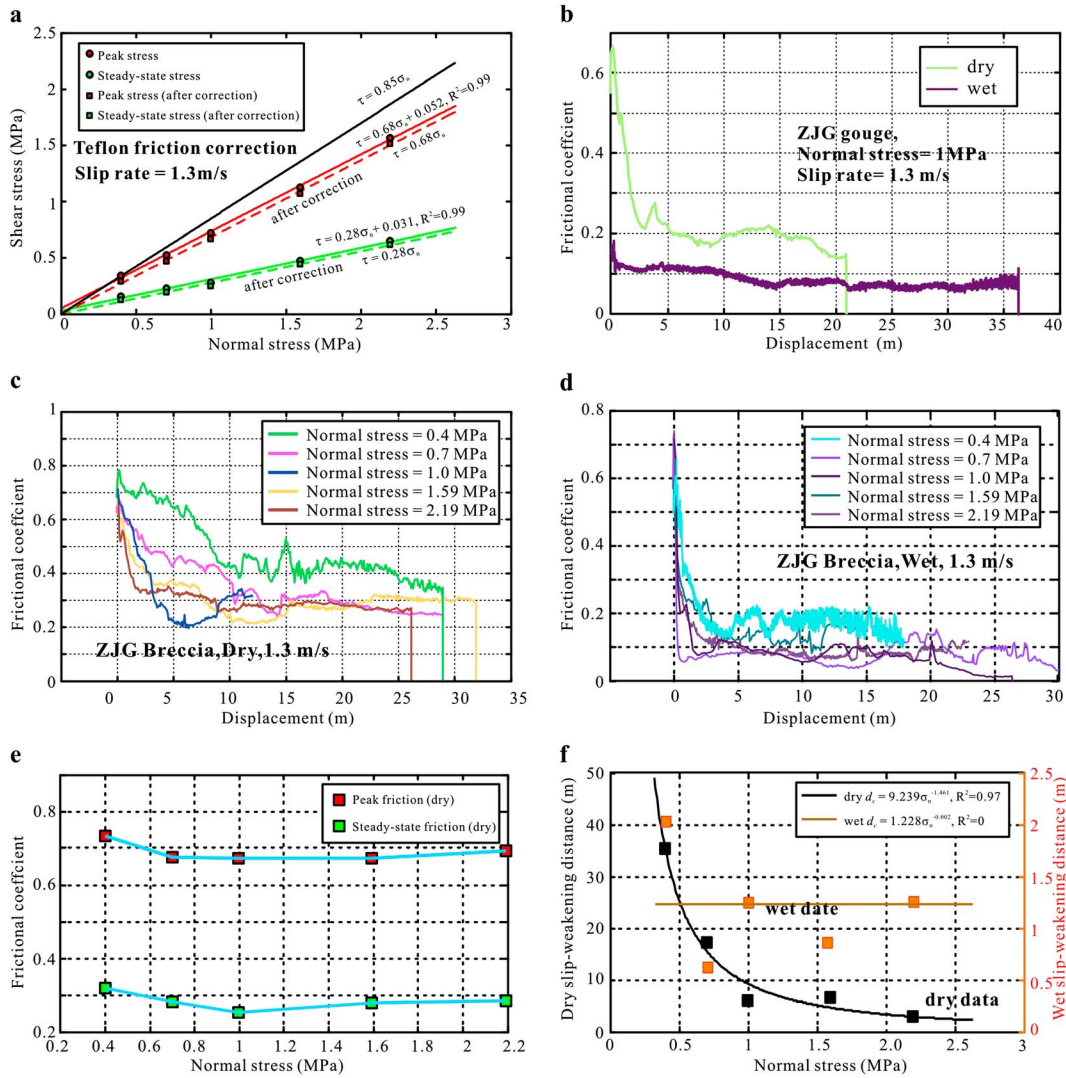
Figure 4. High-velocity friction results. (a) An example illustrating Teflon friction corrections by the intercept method. (b) Dry and wet friction of the natural fault gouge. (c) Dry and (d) wet friction of simulated gouge crushed from the adjacent fault breccia. (e) Friction coefficient and (f) slip-weakening distance as function of normal stress for simulated gouge crushed from fault breccia under dry and wet conditions. Data points of Figures 4e and 4f are derived from Figures 4c and 4d.

the pores by evacuation and saturating the system with distilled H_2O, (3) measure permeability (together with specific storage) using the pore pressure oscillation method at effective pressure P_{e0}, (4) change confining pressure and determine the resultant porosity change, and (5) repeat steps 3 and 4 after each step change in confining pressure. In this way, a set of data, including permeability, porosity, and specific storage, was obtained for a complete confining pressure cycle for each sample. In our tests, the mean pore pressure was set to be around 14 MPa and the confining pressure was first stepped upward from 20 to 180 MPa and then downward.

[14] The pore pressure oscillation method has been described in detail in previous publications [*Kranz et al.*, 1990; *Fischer and Paterson*, 1992; *Faulkner and Rutter*, 2000; *Bernabé et al.*, 2006], so only a brief description is given here. A sinusoidal oscillating pressure was applied at the upper end of the sample, and the response at the downstream end was recorded (Figure 3b). The early transient signal was removed, and Fourier analysis was carried out to get the amplitude ratio ($0 < \alpha < 1$) and phase delay ($\theta < 0$) between the upstream and downstream signals. Following *Faulkner and Rutter* [2000], permeability (k) and specific storage (S_s) of the sample can be calculated using an iterative method with α and θ as the input data.

[15] Initial porosity (Φ_0) was obtained on the basis of the Boyle-Mariotte theory. The effective pore volume (V_p) of the sample was determined based on the balanced pressure (P_3) obtained by connecting two sealed vessels with known internal volume (V_1, V_2) and pressure (P_1, P_2) (Figure 3c). If ideal gas behavior is assumed for the N_2 used, we have $P_1(V_1 + V_p) + P_2V_2 = P_3(V_1 + V_2 + V_p)$, so V_p can be written as $V_2(P_3 - P_2)/(P_1 - P_3) - V_1$. The volume of V_1 and V_2 was calibrated in advance using a series of hard alloy cylinders with holes of various diameters. Porosity was calculated as $V_p/(V_p + V_{gr})$, where V_{gr} is the grain volume assumed to be

Table 1. Mineralogical Composition of Fault Rocks Collected at Various Distances From the Slip Surface[a]

Lithology	Distance (cm)	Bulk Composition					Clay Composition (Ref. %)			
		Q	Fel	Dol	Cal	Clay	It	I/S	Chl	S%
Coarse breccia	−175[c]	1%	1%	29%	68%	2%		95%	5%	5
Yellow fine breccia	−6	2%	1%	67%	29%	2%	39%	55%	6%	10
Thin black gouge[b]	0	43%	1%	19%	7%	30%	22%	64%	14%	38
Gray gouge	0	29%	2%	27%	7%	35%	3%	83%	14%	36
Yellow fine breccia	4	6%		62%	24%	8%	19%	73%	8%	33
Gray coarse breccia	60	43%	33%		8%	16%		51%	49%	5

[a]Notation of symbols for minerals are Q for quartz; Fel, feldspar; Cal, calcite; Dol, dolomite; It, illite; I/S, mixed layer of illite and smectite; Chl, chlorite; S%, the percentage of smectite in I/S.
[b]The thin black gouge occurs adjacent to the gray zone, and both of them are taken as the slip zone material.
[c]Being negative means on the hanging wall.

constant. We made this measurement at different pressures up to 3 MPa but found no dependence of measured porosity on pressure. This means that there can be no significant absorption effect. The average value was taken as the initial porosity. Uncertainty in this measurement is below 0.3%.

[16] A new approach was developed to determine the porosity change at each step change in confining pressure. In previous studies, pore volume changes were measured by high-precision volumometers with pore pressure being controlled at a constant value [e.g., *Ko et al.*, 1997]. In this study, they were evaluated from the fluid pressure change in a closed system (Figure 3d), assuming that the entire volume change represents the pore volume change in the specimen, based on the fact that the compressibility of individual grains is much smaller than the bulk compressibility [*Wibberley and Shimamoto*, 2005]. In each run, we first closed valve $\#_1$ and $\#_2$ to obtain a closed system, incorporating the core sample and the pipelines connecting the microvolumometer and the pressure transducer (Figure 3d). Confining pressure was then stepped upward/downward from P_{c_i} to P_{c_f}, resulting in shrinkage/swelling of the sample and thus pressurization/depressurization of the pore fluid from P_{d_i} to P_{d_f}, as measured by the pressure transducer. The pore volume change (ΔV_p) can be calculated by integrating B_d^* over the pore pressure change, that is, $\Delta V_p = \int_{P_{d_i}}^{P_{d_f}} B_d^* dp$, where B_d^* is the sample storage plus the storage of downstream reservoir (B_d). As the most important parameter in processing the data, B_d was precisely determined using the specially designated microvolumometer, composed of a needle valve and a high-precision linear voltage differential transducer (Figure 3d).

[17] Specific storage can be gained simultaneously with permeability by the pore pressure oscillation method. However, this method may suffer uncertainties [*Bernabé et al.*, 2004, 2006]. Alternatively, in poroelasticity theory, specific storage is related to porosity, fluid (β_f) and mineral compressibility (β_m), and drained bulk framework compressibility (β_b) as follows [*Brace et al.*, 1968]:

$$S_s = \beta_b + \Phi\beta_f - (1 + \Phi)\beta_m. \qquad (1)$$

[18] With the assumption that β_m is negligible in comparison to that of the sample as a whole, β_b can be approximated by finding the pore volume change per unit effective pressure change and dividing this by the sample volume at the start of each upward or downward pressurization step. This result

was an "averaged" compressibility over the P_c range of the step, which was assumed to represent the β_b at the median P_c of the step [*Wibberley*, 2002].

4. Results

4.1. Mineralogical Composition

[19] Mineralogical data obtained for the samples investigated are presented in Table 1. XRD analysis identified quartz, dolomite, and calcite as major minerals and feldspar as minor mineral. Clay minerals in the samples of less than 2 µm in size are composed mainly of mixed layers of illite-smectite (I/S), illite, and chlorite, with no detectable smectite. Compared with nearby breccia samples, black and gray gouges are abundant in clay minerals and poor in calcite content, and mixed layers of illite-smectite are the dominant clay mineral with a percentage of smectite of 36%–38%. The thin black gouge, which is considered having accommodated most of the fault motion, has a composition similar to the gray one, except for a higher quartz and illite content (43% and 6.6% vs. 29% and 1%, Table 1).

4.2. High-Velocity Friction Data

[20] All friction data were corrected for friction exerted by the Teflon sleeve against the host gabbro block. This was done using the intercepts determined from a set of experiments performed on the material under various normal stresses of 0.4, 0.7, 1.0, 1.59, and 2.19 MPa (Figure 4a). Following the method of *Togo et al.* [2011], the Teflon friction was set to evolve with displacement, linearly increasing from zero to peak friction and then exponentially decreasing to a steady state value. Considering that the normal stress did not act on the Teflon-gabbro interface, the friction was inferred to be independent of the normal stress imposed.

[21] The dry tests displayed frictional behavior that has been recognized in numerous previous studies of fault material at seismic slip rates. They are characterized by a peak friction followed by dynamic weakening to a steady state level (Figures 4b and 4c). The peak (μ_p) and steady state (μ_{ss}) friction are around 0.65, 0.07 for the gray gouge (Figure 4b) and 0.68, 0.28 for the fault breccia sample (Figure 4c). Under the normal stresses investigated, 5 to 8 m displacement is required to achieve a steady state slip. The postpeak slip-weakening curves obtained in our experiments (Figures 4b and 4c) are similar to previous results for fault gouges [e.g., *Brantut et al.*, 2008], as described in the empirical equations proposed by *Mizoguchi*

Table 2. Measured Mineralogical, Frictional, and Transport Properties of Fault Rocks for Numerical Modeling

Parameters	Symbol	Values or Functions	Units
Content of Reacting Components			
Smectite content of gouge[a]	ω_{sm}	10.7%	wt %
Dolomite content of gouge	ω_{do}	27%	wt %
Smectite content of adjacent fine breccia	ω_{sm}	1.9%	wt %
Dolomite content of adjacent fine breccia	ω_{do}	62%	wt %
Smectite content of coarse breccia	ω_{sm}	0.4%	wt %
Dolomite content of coarse breccia	ω_{do}	0	wt %
Frictional Parameters			
Peak friction of dry gouge	μ_p	0.65	
Steady state friction of dry gouge	μ_{ss}	0.17	
Slip-weakening distance of dry gouge[b]	d_c	$4.0 \times P_e^{(-1.17)}$	m
Transport Properties			
Permeability of fault gouge (Run 4)[c]	k^u	$9.85 \times 10^{-19} P_e^{(-1.3939)}$	m^2
	k^d	$2.31 \times 10^{-20} P_e^{(-0.7189)}$	m^2
Porosity of fault gouge (Run 4)	Φ^u	$0.325 P_e^{(-0.2661)}$	
	Φ^d	$0.143 P_g^{(-0.1141)}$	
Compressibility of fault gouge (Run 4)	β_b^u	$5.43 \times 10^{-8} P_e^{(-1.0773)}$	Pa^{-1}
	β_b^d	$1.66 \times 10^{-8} P_e^{(-1.0752)}$	Pa^{-1}
Permeability of adjacent fine breccia (Run 36)	k^u	$7.82 \times 10^{-18} \exp(-0.02829(P_e - 1))$	m^2
	k^d	$4.15 \times 10^{-19} P_e^{(-0.3532)}$	m^2
Porosity of adjacent fine breccia (Run 36)	Φ^u	$0.196 \exp(-0.002153(P_e - 1))$	
	Φ^d	$0.182 P_e^{(-0.05120)}$	
Compressibility of adjacent fine breccia (Run 36)	β_b^u	$4.24 \times 10^{-9} P_e^{(-0.5485)}$	Pa^{-1}
	β_b^d	$6.28 \times 10^{-9} P_e^{(-0.8351)}$	Pa^{-1}
Permeability of coarse breccia (Run 13)	k^u	$1.80 \times 10^{-16} \exp(-0.01642(P_e - 1))$	m^2
	k^d	$3.19 \times 10^{-17} P_e^{(-0.1991)}$	m^2
Porosity of coarse breccia (Run 13)	Φ^u	$0.195 \exp(-0.002555(P_e - 1))$	
	Φ^d	$0.164 P_e^{(-0.04571)}$	
Compressibility of coarse breccia (Run 13)	β_b^u	$3.77 \times 10^{-9} P_e^{(-0.5072)}$	Pa^{-1}
	β_b^d	$1.88 \times 10^{-8} P_e^{(-1.2581)}$	Pa^{-1}

[a]The content of smectite is calculated by multiplying the clay content by the relative content of I/S and by the percentage of smectite (S%) within I/S, with values being given in Table 1.

[b]Slip-weakening distance (d_c) is extrapolated to the targeted effective stress by a power-decay equation, in which P_e is the effective pressure in unit of MPa and the decay coefficient is from the yellow breccia sample.

[c]Superscript "u" and "d" denote upward and downward pressurization path. The evolution of k as a function of pore pressure change (Δp) at a given depth (with initial effective pressure of P_{e0}) is calculated as $k(\Delta p) = k^d(P_{e0} - \Delta p) - k^d(P_{e0}) + k^u(P_{e0})$ (see explanation in text). A similar formula also applies for the evolution of porosity, $\Phi(\Delta p) = \Phi^d(P_{e0} - \Delta p) - \Phi^d(P_{e0}) + \Phi^u(P_{e0})$. Specific storage is given as $S_s(\Delta p) = \beta_b^d(P_e) + \Phi(P_e)\beta_f - (1 + \Phi(P_e))\beta_m$, where P_e equals to $P_{e0} - \Delta p$. Note that the equations for transport properties only apply for P_e ranging from 5 to 165 MPa. The properties at low P_e are obtained by extrapolation of low pressure data (5–15 MPa) using the exponential law.

et al. [2007] or *Di Toro et al.* [2011]. These equations are equivalent to one another and only differ in how they define the critical slip-weakening distance (d_c). In our study, d_c is defined following *Mizoguchi et al.* [2007] as the distance over which stress drop reduces to 5% of the initial value:

$$\mu_d = \mu_{ss} + \left(\mu_p - \mu_{ss}\right) \exp[\ln(0.05)d/d_c]. \qquad (2)$$

[22] Here μ_d is the dynamic friction, and d is the displacement. The value of μ_p corresponded to the value observed at the peak stress, while μ_{ss} and d_c were determined using the fitting method. The corresponding best fit results for the gouge sample are listed in Table 2. The peak and steady state friction seem to be only weakly dependent of the normal stress (Figure 4e), consistent with previous studies [e.g., *Mizoguchi et al.*, 2007]. By contrast, the slip-weakening distance decreases notably with increasing normal stress, which can be fitted empirically by a power law, as labeled in Figure 4f.

[23] In the cases of the wet experiments, the natural gouge was characterized by rapid attainment of steady state and by little or no dynamic weakening (Figure 4b). The steady state friction was lower than that under dry but otherwise the same conditions. For the fault breccia sample, the slip-weakening process is very rapid (Figure 4d), with d_c around 0.6 to 2.0 m under the normal stress investigated, which is much smaller than that obtained for the dry samples under the same normal stress (Figure 4f). Moreover, no systematic relationship between d_c and normal stress was evident (Figure 4f).

4.3. Transport Property Data

[24] Our logarithmic permeability, porosity, and logarithmic specific storage results are plotted against the effective pressure (P_e) in Figure 5. The specific storage data is derived from equation (1). The permeability curves show a rapid decrease as P_e increases to 165 MPa, while the curves along the downward pressurization path show a slight increase as P_e is reduced from 165 to 30 MPa, followed by a rapid increase as 7 MPa is approached. The permeability of different fault rocks can vary by up to 5 orders of magnitude under the same P_e. The permeability of individual samples can be reduced by 2 to 4 orders of magnitude by an increase in P_e from 7 to 165 MPa. The gray gouge has the lowest permeability (as low as 7.3×10^{-22} m^2 at a P_e of 165 MPa) compared with the other fault rocks, which have permeability greater than 1.0×10^{-19} m^2, except for the microfractured limestone. The permeability of the country rock (intact limestone) at a
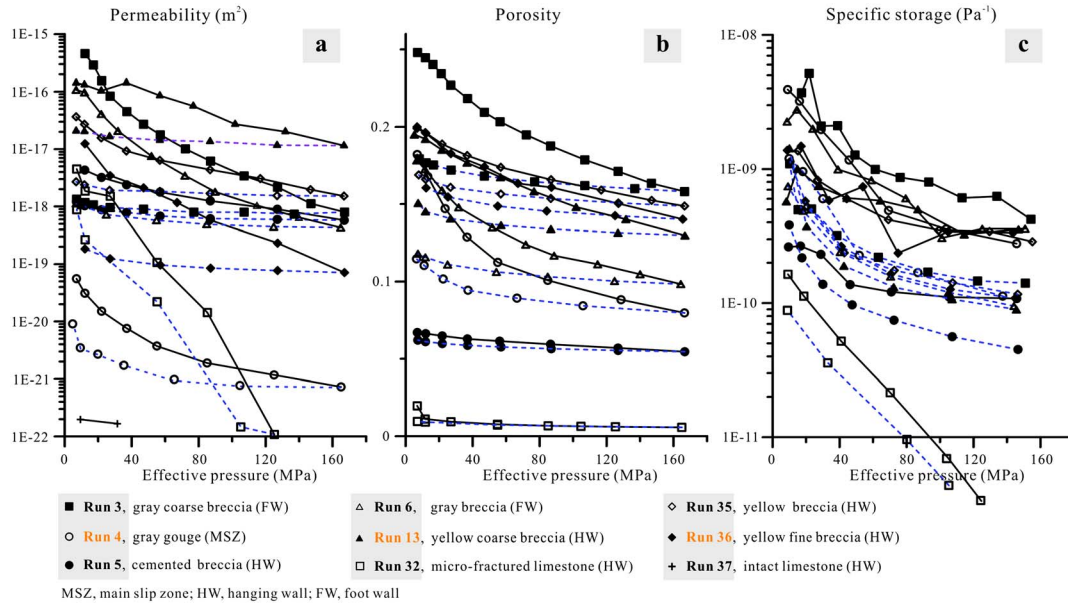
Figure 5. Transport property results. (a) Permeability, (b) porosity, and (c) specific storage of various fault rocks collected from the ZJG exposure. Solid black and dashed blue lines indicate the upward and downward pressurization paths, respectively. Specific storage is given by using fluid compressibility of $4.3 \times 10^{-10}\,\mathrm{Pa}^{-1}$ [*Fine and Millero*, 1973]. Results of the hanging wall rocks (Runs 4, 13, and 36) are used for numerical modeling, and the detailed fitting equations are given in Table 2.

P_e of ~ 10 MPa is close to the detection level ($1.0 \times 10^{-22}\,\mathrm{m}^2$) of our experimental configuration, so we did not run a complete P_e-cycling test on it.

[25] Initial porosities (at a P_e of 7 MPa) range between 2.1% and 25% for the different rocks across the fault zone. Similar to permeability, the fault gouge sample shows rapid decay with increasing P_e (Figure 5b). The microfractured limestone displays the lowest porosity (0.7% at a P_e of 165 MPa), which is followed by the cemented breccia (5.5%) and the gray gouge (8.0%). The specific storage curves are clearly separated between the upward and downward pressurization paths (Figure 5c), and the curves are roughly parallel to each other. This results from the bulk framework compressibility (see equation (1)), which has much smaller value along the downward pressurization path relative to along the upward one. Initial values of specific storage range between 1.8×10^{-10} and 5.3×10^{-9} Pa^{-1}. Most specific storage values fall in the range of 5.0×10^{-11} to $5.0 \times 10^{-9}\,\mathrm{Pa}^{-1}$. The fractured limestone shows the highest pressure sensitivity, and its value falls below $1.0 \times 10^{-11}\,\mathrm{Pa}^{-1}$ under 100 MPa.

[26] Fluid flow simulation requires empirical equations reflecting the relationship between transport properties and depth (or effective pressure). The slopes of all curves become gentler with increasing effective pressure, implying declining pressure sensitivities with depth. To describe this, an exponential law [*David et al.*, 1994] in the form of $X = X_0 \exp(-q(P_e - 1))$ and a power law [*Shi and Wang*, 1986] in the form of $X = X_0 P_e^{-r}$ have been used to fit these data. Here X represents transport properties such as permeability, porosity, and framework compressibility; X_0 is the value at a P_e of 1 MPa; and q and r are material constants indicating pressure sensitivity. Which relation was

adopted for individual materials depends on the goodness of fit. Most of the data in Figure 5 do not plot on straight lines described by the exponential law, particularly for the gouge sample; the data of which fits favorably well with the power law, consistent with the previous studies on clay-rich samples [*Shi and Wang*, 1986; *Mizoguchi et al.*, 2008]. Fitting results used for modeling are presented in Table 2.

5. Numerical Analysis of Coseismic Thermochemical Pressurization

[27] During an earthquake, frictional heating generated in the slip zone will induce a temperature rise and thus a pore pressure rise, as well as possible activation of chemical reactions. In the following, we report numerical modeling of the coseismic slip-weakening process, treating the slip zone as infinite in extent and including thermochemical effects. We use local slip history data for the Wenchuan earthquake and lab friction data to compute the heat source. We use measured in situ transport properties and previous data on reaction rate constants for quantifying the decomposition reactions. Strongly state-dependent thermodynamic properties of pore fluid are also incorporated into our models.

5.1. Governing Equations

[28] The coupled equations for energy and fluid mass conservation that govern the coseismic slip process are well established [*Lachenbruch*, 1980; *Noda and Shimamoto*, 2005; *Rice*, 2006]. Coseismic chemical reactions have also recently been incorporated [*Sulem and Famin*, 2009;

Table 3. Kinetic Models and Parameters of Reactions Involved in This Study[a]

Reactions	$f(\xi)$	ΔH	A	E_a	χ	ΔV	References
Dehydration of smectite	$1 - \xi$	−43	553	32.2	2	19.4	*Bray and Redfern* [1999]; *Noyan et al.* [2008]
Dehydroxylation of smectite	$1 - \xi$	−132	8.8	50.7	1	0	*Tanikawa et al.* [2009]; *Noyan et al.* [2008]
Smectite-to-illite transformation *	$(1 - \xi)^2$	−100	1.57×10^{-5}	117.2	0	0	*Huang et al.* [1993]; *Brantut et al.* [2010]; *Zhou* [1993]
Decarbonation of dolomite	$(1 - \xi)^{2/3}$	−178	2.68×10^7	187	1	24.0	*Criado et al.* [1995]

[a]ξ, the reacted fraction; $f(\xi)$, the reaction function; ΔH, molar enthalpy change of the reaction in unit of kJ mol^{-1}; A, the reaction rate constant in unit of s^{-1}; E_a, the activation energy in unit of kJ mol^{-1}; χ, the mole number of fluid that could be lost by a certain reaction for 1 mol reactant; ΔV, solid volume reduction (%) caused by the reaction.

Tanikawa et al., 2009; *Brantut et al.*, 2010], yielding the following description of this highly coupled system:

$$\frac{\partial T}{\partial t} = \frac{K}{\rho c} \frac{\partial^2 T}{\partial x^2} + \frac{Q_{so}}{\rho c} + \frac{Q_{si}}{\rho c} \qquad (3)$$

$$\frac{\partial p}{\partial t} = \frac{1}{S_s} \left(\frac{\partial}{\partial x} \left(\frac{k}{\eta} \frac{\partial p}{\partial x} \right) \right) + \frac{\phi(\alpha_f - \alpha_m)}{S_s} \frac{\partial T}{\partial t} + \frac{\Omega_{de}}{S_s}. \qquad (4)$$

[29] In equation (3), T is the temperature, t is the time, K is the thermal conductivity, ρ is the bulk density, c is the specific heat capacity, Q_{so} is the heat source per unit volume generated by frictional heating, and Q_{si} is the heat sink per unit volume by chemical reactions. In equation (4), p is the pore pressure, and k, Φ, and S_s are the intrinsic permeability, porosity, and specific storage, respectively. Further, η is the dynamic viscosity of fluid, α_f and α_m are the thermal expansivities of the fluid and individual grains, respectively, and Ω_{de} is the fluid generation rate per unit volume by chemical reactions.

[30] The symbols, their definitions, and corresponding values of variables involved are listed in Tables 2 and 3. Important points in relation to the governing equation are stated below:

[31] 1. Frictional work done by an earthquake can be distributed among frictional heating [*Rice*, 2006], chemical reactions [e.g., *Hamada et al.*, 2009], and grain comminution [*Ma et al.*, 2006]. In the absence of appropriate fracture energy data, only the former two facts are considered in our modeling. Uniform shearing rate within a slip band is assumed, and the heat production rate is then given by

$$Q_{so} = \tau \dot{\gamma} = \mu_d(\sigma_n - \bar{p}) \frac{V}{W}. \qquad (5)$$

where $\dot{\gamma}$ is the shear rate, V is the slip velocity, and W is the thickness of the slip band. As pointed out by *Sulem et al.* [2007], the gradient of shear resistance (τ) induced by coseismic slip acceleration is relatively small (in orders of 10^{-2} MPa/m), so the variation of τ within a slip band can be neglected and mechanical equilibrium can be assumed. The shear resistance is thus taken as linearly proportional to the mean effective normal stress ($\sigma_n - \bar{p}$) inside the slip band [*Sulem et al.*, 2007; *Brantut et al.*, 2010] and set to be zero for overshooting cases ($\bar{p} > \sigma_n$). The heat consumed by chemical reactions is expressed as

$$Q_{si} = \sum \frac{\omega(1 - \phi)\rho_s \Delta H}{M} \frac{\partial \xi}{\partial t}. \qquad (6)$$

Here $\sum$ represents summation of all involved reactions. The term ΔH represents the molar enthalpy change of reaction (kJ mol^{-1}) and is negative when endothermic, ω and M are the wt % content and molar mass of the reactant contained

in the gouge sample, ρ_s is the average density of solid minerals, ξ is the accumulative reacted mass fraction of the reactant through time, and its time derivative $\partial \xi / \partial t$ expresses the reaction kinetics.

[32] 2. Besides thermal effects, some chemical reactions influence evolution of pore pressure by fluid mass production through dehydration or decarbonation ($\Omega_{de} = \Omega_{dehy} + \Omega_{decar}$). Reactions can also involve volume change in the solid phases. For example, dehydration of smectite can produce a solid volume reduction of up to 47% [*Vrolijk and van der Pluijm*, 1999]. Such reduction is associated with lattice collapse and is expected to yield porosity change in bulk rocks [*Wong et al.*, 1997]. Assuming that 1 mol hydrate converts to 1 mol dehydrate, losing χ mol water and producing a volume reduction in solid phase ΔV, the effective fluid generation rate can be expressed as

$$\Omega_{de} = \sum \omega(1 - \phi) \left(\frac{\chi M_{H_2O}}{M_{hy}} \frac{\rho_s}{\rho_f} - \Delta V \right) \frac{\partial \xi}{\partial t}. \qquad (7)$$

where M_{H_2O} and M_{hy} are the molar masses of the pore fluid (H_2O) and the hydrous mineral, respectively, and ρ_f is the density of the pore fluid. In this expression, evolutional porosity is considered. Aside from this, such an expression is similar to that proposed by *Brantut et al.* [2010] for a general chemical reaction. Except for the coupled thermal effect, equation (4) is similar to the equation of *Wong et al.* [1997] for the dehydration system. The decarbonation reaction is treated in a similar way, giving an effective fluid release rate:

$$\Omega_{decar} = \sum \omega(1 - \Phi) \left(\frac{\chi M_{CO_2}}{M_{car}} \frac{\rho_s}{\rho_{CO_2}} - \Delta V \right) \frac{\partial \xi}{\partial t}, \qquad (8)$$

where M_{CO_2}/M_{car} is the ratio between the molar mass of CO_2 and the carbonate minerals, and ρ_{CO_2} is the density of CO_2 in fluid phase (Figure A1). Note that once CO_2 is generated, the pore fluid will become a CO_2-H_2O binary system. In our modeling, we treated the CO_2 and H_2O phases separately, since volumetric contraction due to mixing is only a few percentages, according to the model given by *Hu et al.* [2007]. The effect of the increased density of the mixture was simulated by adjusting ΔV in equation (8). In addition, dynamic dilatancy due to fault surface irregularities or damage production can cause an instantaneous rise in porosity [*Samuelson et al.*, 2009]. However, this effect is expected to be most marked at the early stage of slip and can be simulated by reducing ambient pore pressure [*Rice*, 2006].

[33] 3. Various chemical reactions have been reported to have occurred during fault motion, including dehydration,

dehydroxylation, metamorphic transformation of clay minerals [e.g., *Hirono et al.*, 2008], and decomposition of organic material [*Ikehara et al.*, 2007] and carbonate minerals [*Smith et al.*, 2011]. The kinetics of chemical reactions is commonly expressed by relations of the form

$$\partial \xi / \partial t = f(\xi) \kappa(T). \tag{9}$$

where $f(\xi)$ is the kinetic function determined by the active reaction mechanism (Table 3). Temperature-dependent reaction rate is adopted following an Arrhenius law, $\kappa(T) = A \exp(-E_a/RT)$, where A is the rate constant (s^{-1}), E_a is the activation energy for the reaction (kJ mol^{-1}), and R is the gas constant (8.31 J K^{-1} mol^{-1}). The effect of pressure and fluid chemistry on reaction kinetics is neglected because no data are available.

5.2. Representative Parameter Values

[34] Only the parameters to which the model is particularly sensitive are discussed here. Reaction kinetics determines to what extent a reaction can occur in a given time. Mineralogical analysis revealed abundant smectite-rich I/S in the gouge sample. As a candidate for dehydration, smectite contained in I/S is treated chemically the same as pure smectite, which, unless otherwise stated, is assumed to carry one interlayer of H_2O in the unit lattice cell. Losing it can cause a volume reduction of 19.4%, dictated by the change of basal spacing (d_{001}) from the hydrated to dehydrated state (d_{001} are 100 and 124 nm, respectively [*Huang et al.*, 1994]). The reactions of smectite dehydroxylation and transformation from dehydrated smectite to illite are assumed to cause no solid volume change, considering the tiny difference in their densities (Table 3). A first-order kinetic function is adopted for dehydration and dehydroxylation, $f(\xi) = 1 - \xi$ [*Bray and Redfern*, 1999]. Since both the solid and solution phases are involved in the reaction of smectite-to-illite transformation (e.g., uptake of K$^+$ from aqueous phase), the kinetic law is complex and expressed as $-dS/dt = \bar{A} \exp(-E_a/RT)[\text{K}^+]S^2$ [*Huang et al.*, 1993], where S is the relative molar fraction of smectite in the I/S, $\bar{A}$ is the frequency factor given as 8.08×10^{-4} s^{-1} M^{-1} and [K$^+$] is the concentration of potassium (M) present in aqueous solution. To express uniformly as a function of ξ as equation (9), S is substituted by $S_0(1 - \xi)$, where S_0 is the initial relative molar fraction of smectite. This gives $f(\xi) = (1 - \xi)^2$ and $A = \bar{A}[\text{K}^+]S_0$. In our modeling, S_0 is 36% from the mineralogical results (Table 1) and [K$^+$] is 5.4×10^{-2} M, as measured for the interstitial fluid chemistry of the Triassic Xujiahe group at $\sim$ 2016 m depth in Wusheng, Sichuan by *Zhou* [1993]. Substituting these values into the expression of A gives a value of 1.57×10^{-5} s^{-1}. Besides I/S changes, XRD analysis also identified dolomite as a major mineral. Dolomite begins to decompose at 550°C [*Han et al.*, 2007], and the products are Ca-calcite + periclase or lime + periclase [*De Paola et al.*, 2011]. In view of the high content of dolomite and the large temperature buffering effect of the endothermic process of decarbonation reaction [*Sulem and Famin*, 2009; *Brantut et al.*, 2011], decarbonation in our study is taken as referring in particular to the reaction CaMg $(CO_3)_2 \rightarrow CaCO_3 + MgO + CO_2$. The kinetic function used is $f(\xi) = (1 - \xi)^{2/3}$ [*Criado et al.*, 1995], and ΔV is assumed

to be 24% on the basis of the mass reduction in solid phases. All reactions involved and related kinetic parameters are summarized in Table 3.

[35] Frictional and transport properties of the fault gouge are further key parameters deciding the TP effect [*Wibberley and Shimamoto*, 2005]. Dynamic friction is set to evolve with displacement following the laboratory-derived empirical equations for dry samples presented in Table 2. In doing this, it is assumed that no significant TP effect occurred in our dry experiments [*Tanikawa et al.*, 2012]. This is later supported by numerical modeling of our high-velocity experiments (section 6.2). The applied normal stress in our friction experiments was much lower than the effective normal stress expected in situ during fault motion, which on the basis of previous modeling studies [*Tanikawa et al.*, 2009] is thought to lie in the range from initial effective pressure to a nearly unconfined condition. Fortunately, the peak and steady state friction are not sensitive to normal stress in the range investigated here (Figure 4e). Also, as a first-order estimate, the slip-weakening distance can be extrapolated to high normal stress using the decay equation given in Table 2, while for low normal stress (< 0.4 MPa), it is set to be constant. Transport properties, including permeability and porosity, are set as a function of P_e as in Table 2. We took the dependences on increasing and decreasing pressure from our results (Figure 5), assuming that the sensitivity of these quantities to decreasing P_e from the initial P_e value imposed is independent of that value. Previous P_e-cycling experiments [*Faulkner and Rutter*, 2000; *Noda and Shimamoto*, 2005] have shown that this is a reasonable assumption. Specific storages derived from the depressurization curves (the dashed lines in Figure 5c) were used, considering similar evolutional trend in effective pressure for a TP process [*Wibberley and Shimamoto*, 2005]. See detailed expressions of these properties at a given depth in the notation of Table 2. Note that the dynamic friction data were obtained under constant normal stress (without confinement) and that the transport property data were obtained under hydrostatic loading (without nonhydrostatic loading); therefore, the stress states do not exactly correspond to one another or to the in situ condition investigated in our modeling. Of course, each set of the data by itself is quite relevant to the problem at hand.

[36] The rate of fluid transport out of the fault zone is also dependent on the evolution of pressure and temperature (PT) through changes in fluid properties. For example, with increasing temperature, pore fluid becomes less viscous, facilitating fluid transportation. In fact, the PT conditions during faulting can vary over a large range, and the pore fluid may even undergo phase changes [*Tanikawa et al.*, 2009; *Sulem and Famin*, 2009] as well as changes in gas phase solubility [*Sabirzyanov et al.*, 2003]. The fluid properties can correspondingly undergo large changes (Figure A1). To model the in situ situation more realistically, state-dependent fluid properties (SDFP), i.e., density, compressibility, thermal expansivity, and viscosity, are introduced. These properties are interpolated as functions of PT and from the basic thermophysical property database of water (see Appendix A for details). The values of specific heat capacity and thermal conductivity are from *Tanaka et al.* [2006] (Table 4).

Table 4. Parameters Used in the Modeling

Parameter	Symbol	Value[a]	Units	Reference
Slip velocity	V	SH	m s^{-2}	*Zhang et al.* [2009]
Time span of slip	t_s	22	s	*Zhang et al.* [2009]
Slip band thickness	W	20 (0.3–20)	mm	Measurement in this study
Specific heat capacity	c	800	$\text{J kg}^{-1}\text{K}^{-1}$	*Tanaka et al.* [2006]
Heat conductivity	K	2	$\text{W m}^{-1}\text{K}^{-1}$	*Tanaka et al.* [2006]
Thermal gradient	dT/dz	21	$°\text{C km}^{-1}$	*Mori* [2010]
Bulk density	ρ	2.5×10^3	kg m^{-3}	Measurement in this study
Solids density	ρ_s	2.7×10^3	kg m^{-3}	Measurement in this study
Fluid density	ρ_f	SDFP (or 1.0×10^3)	kg m^{-3}	NIST
Dynamic viscosity	η	SDFP (or 1.26×10^{-4})	Pa s	NIST (or *Rice* [2006])
Thermal expansivity of fluid	α_f	SDFP (or 5.0×10^{-4})	K^{-1}	NIST (or *Fine and Millero* [1973])
Compressibility of fluid	β_f	SDFP (or 4.3×10^{-10})	Pa^{-1}	NIST (or *Fine and Millero* [1973])
Thermal expansivity of grains[b]	α_m	2.2×10^{-5}	K^{-1}	*Bayer* [1973]
Compressibility of grains[c]	β_m	1.2×10^{-11}	Pa^{-1}	*Birch* [1966]
Hydrostatic/lithostatic pressure	λ	0.4 (0.1–0.5)		

[a]Values in parentheses are used for parametric analysis. SH, from inferred slip history by seismological inversion;
[b]The coefficient of thermal expansivity of quartz was used in place of that of the minerals contained in fault rocks.
[c]The compressibility of mica was used in place of that of the minerals contained in fault rocks.
SDFP, state-dependent fluid properties (Appendix A); NIST, from website http://webbook.nist.gov/chemistry/fluid/.

5.3. Modeling Strategy

[37] A laterally infinite and homogeneous, plate-like planar fault model is used, assuming that all quantities, including frictional and hydraulic properties of the fault rocks, change only in the direction normal to the fault plane. In accordance with the real fault structure (Figure 2c), a symmetric geometrical model is constructed, consisting of the central fault gouge (2 cm thick), the adjacent fine breccia zones (9 cm thick for each side), and the coarse breccia zones (40 cm thick for each side) outside. As illustrated in Figure 6f, the geometrical model is meshed into 608 elements in total, 32 of which occupy the gouge zone.

[38] Boundary and initial conditions are set as below. We take zero-flux boundaries for the fluid and temperature fields. The fault model is sufficiently wide to be "infinite" relative to the temperature and fluid fields, with respect to the time span investigated. Uniform hydrostatic initial condition, unless otherwise stated, is assumed by letting λ (the ratio of pore pressure to lithostatic pressure) be 0.4. Uniform initial temperature is assigned on the basis of the local geothermal gradient (Table 4). As shown in Figures 2c and 2d, two kinds of gouge occur in the fault center, the gray gouge and the thin black gouge. Mineralogical and chemical analyses [*Chen et al.*, 2013] have revealed the black gouge to be the material having accommodated most of the coseismic displacement and having formed from the gray gouge. Therefore, the gray gouge is taken as the initial material before the Wenchuan earthquake. Initial mineral composition of the gray gouge and the fine and coarse breccia zone is set according to the XRD data for these materials (Table 2).

[39] The slip history computed from the waveshape inversion of seismological data [*Zhang et al.*, 2009] is used to specify the heat source. The nearest inversion result is 3.8 km northeast of the exposure studied. The subsurface slip history is extrapolated from the data for 3.1 km depth, constraining the total displacement to be equal to that measured at the surface by geological surveying (Figure 1c). The slip histories at various depths were linearly interpolated from the curves given in Figure 1e. Our modeling addresses a time interval totaling 2500 s from the onset of the slip. In accordance with the real slip history

(Figure 1e), the time step is set to be 0.05 s in the first 25 s (coseismic stage) and is then changed to 0.5 s for the postseismic stage.

[40] The coupled partial differential equations (PDEs) describing energy balance, fluid mass transport, and chemical reactions are solved using the finite element software COMSOL (version 3.5), solving simultaneously for all dependent variables including pore pressure (p), temperature (T), and normalized chemical concentrations (ξ). In other words, all these variables are iterated sequentially until the accumulated (global) error meets both the relative and absolute tolerations represented by the error in each time step. The mean pore pressure inside the slip ($\bar{p}$) has also been taken into the iteration. In each iteration step, it is calculated by integrating the pore pressure over the slip band width and dividing it by the width of the slip band. Nonlinear parameters, i.e., permeability, porosity, specific storage, friction, d_c, and reaction constants, are taken into the iteration procedure as well. Finally, the linear equations (in form of $Ax = b$) assembled from all the coupled PDEs and boundary conditions are solved using a linear system solver (UMFPACK), which uses the nonsymmetric-pattern multifrontal method and direct LU factorization of the sparse matrix A.

5.4. Numerical Results

[41] Our modeling approaches calculate the evolution of pore pressure, temperature, and reactant concentration through time as a function of distance from the slip surface. Dynamic friction and dynamic shear stress are computed versus displacement. The weakening efficiency ($\mu_d(\sigma_n - \bar{p})/\mu_p(\sigma_n - p_0)$), defined as dynamic shear stress divided by initial shear resistance, depends on the evolution of both the friction and the mean pore pressure inside the slip zone. Evolution of the latter is further controlled by the interplay between thermal pressurization of fluid trapped in pores, fluid mass liberation from reactions, and fluid loss by drainage from the heated zone, whereupon we evaluate the contribution of these terms of $\frac{\phi(\alpha_f - \alpha_s)}{S_s}\frac{\partial T}{\partial t}$, $\frac{\Omega_{de}}{S_s}$, and $\frac{1}{S_s}\left(\frac{k}{\eta}\frac{\partial^2 p}{\partial x^2}\right)$ separately. To understand energy partitioning during fault motion, heat
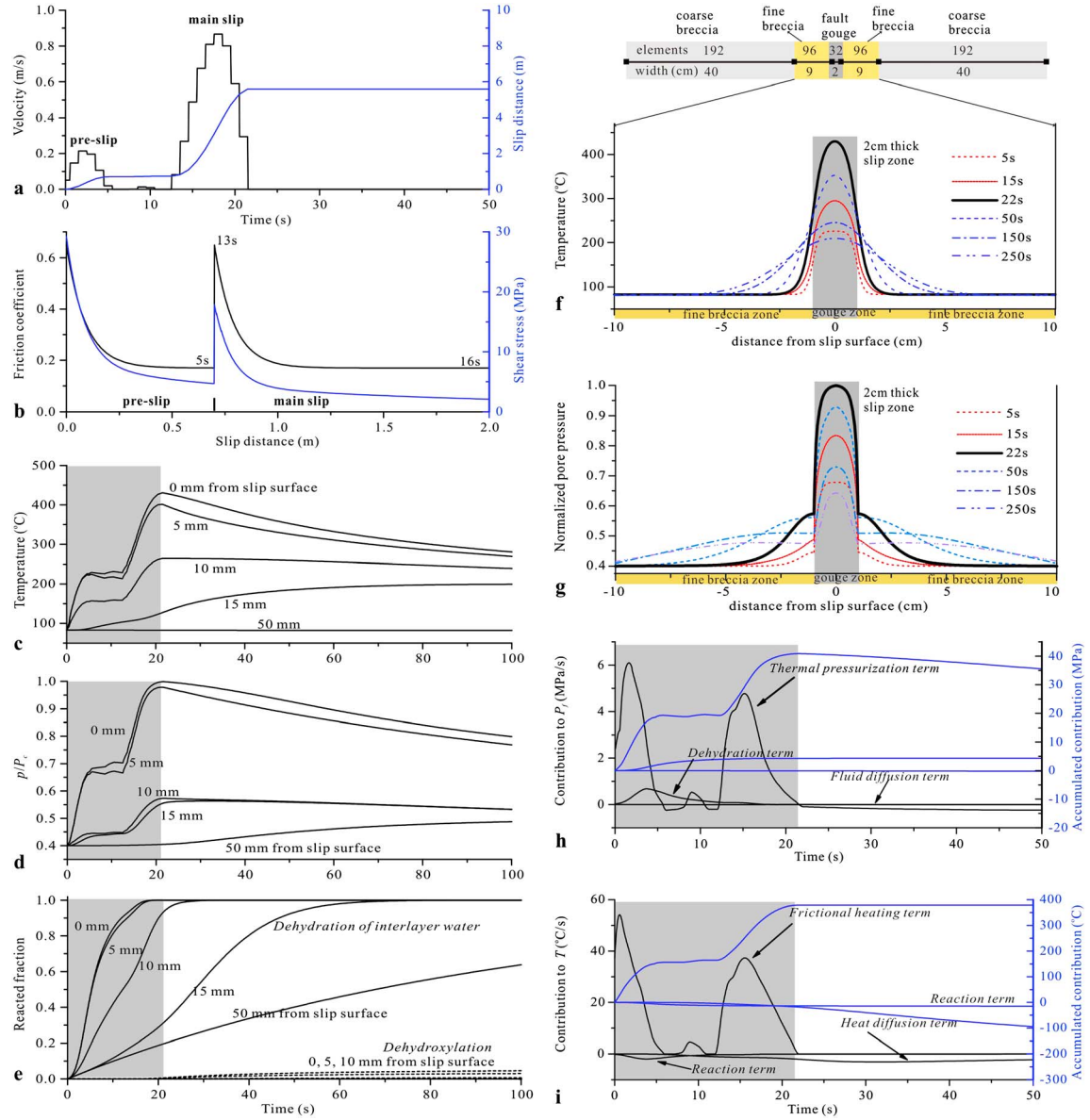
Figure 6. Modeling results of the reference case (Ref). (a) Slip velocity and accumulated displacement with time. (b) The evolution of friction coefficient and shear stress as slip distance. The evolution of (c) temperature, (d) normalized pore pressure, and (e) reacted fraction of reactants with time at various distances from the slip surface. Snapshots of the distribution of (f) temperature and (g) normalized pore pressure across the fault core. (h) Contribution to the temperature rise by thermal pressurization, dehydration, and diffusion, respectively. (i) Contribution to the pore pressure buildup by thermal pressurization, dehydration, and diffusion, respectively. The conditions implied in Ref are explained in the text. The shaded areas in Figures 6c–6e, 6h, and 6j denote the time span of the Wenchuan earthquake, and those in Figures 6f and 6g represent the gouge zone. Simulations are performed on the fault model consisting of the central gouge zone, the fine breccia zone, and the coarse breccia zone (top panel of Figure 6f). To show details at the central portion, the temperature and pore pressure profiles presented (Figures 6f and 6g) only include the gouge zone and the fine breccia zone.

production by friction ($\frac{Q_{so}}{\rho c}$), heat consumption by endothermic reactions ($\frac{Q_u}{\rho c}$), and thermal diffusion ($\frac{K}{\rho c}\frac{\partial^2 T}{\partial x^2}$) are evaluated also. The time integral of each term is computed as well. To illustrate the interplay between frictional heating and fluid pressurization, local pore pressure at the slip surface is plotted against temperature (referred to as *p-T* curve). Representative results are presented in the following (Figure 6).

5.4.1. The Reference Case

[42] First, we show results of the reference case (referred to as *Ref*), in which slip is evenly distributed in a 20 mm thick gouge zone located at 3 km depth, with an ambient temperature of 83°C, confining pressure of 75 MPa, and initial pore pressure of 30 MPa. Other parameters are as for the representative values set in section 5.2. Allowing for two stages of slip, a total displacement of 5.6 m was achieved
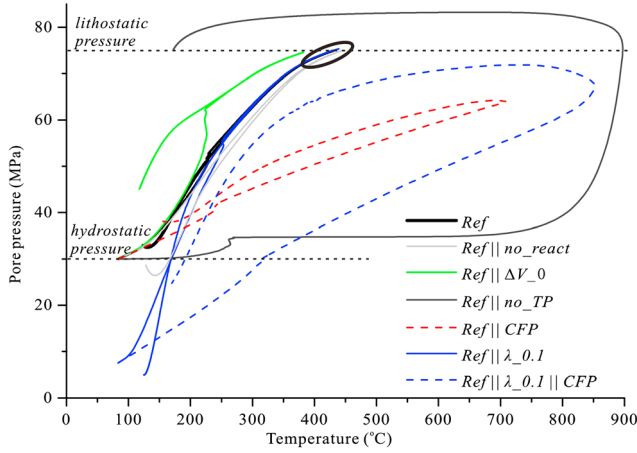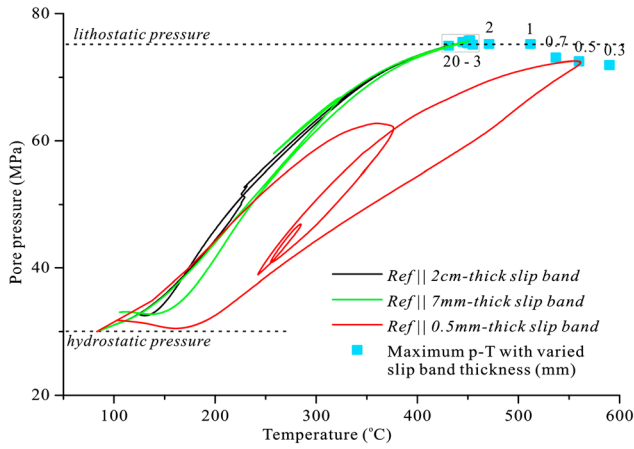
Figure 7. The computed *p-T* curves at the slip center in different cases. Ref, reference case; Ref ‖ no_TP, reference case without thermal pressurization; Ref ‖ no_react, reference case without chemical reactions; Ref ‖ ΔV_0, reference case without considering solid volume reduction due to reaction; Ref ‖ CFP, reference case but using CFP; Ref ‖ λ_0.1, reference case except for λ of 0.1 being used; Ref ‖ λ_0.1 ‖ CFP, reference case but using CFP and λ of 0.1.

in 22 s (Figure 6a). The shear stress first drops from 29.3 to 16 MPa in the preslip stage and then further to 1.1 MPa by the end of the slip (Figure 6b). The shear stress continues to decay when the friction attains steady state (Figure 6b), suggesting involvement of extra weakening mechanism besides frictional weakening of the fault material. By the end of the slip, the maximum temperature on the slip surface reaches 431°C (Figure 6c). The pore pressure closely approaches the lithostatic pressure, but it decays rapidly away from the slip surface (Figure 6d). Smectite contained in the gouge has fully lost its interlayer water by the end of the slip (see the curve for material at 10 mm away from the slip surface in Figure 6e), and dehydroxylation occurs to a limited degree. Snapshots of the fluid pressure and temperature fields in time are also presented (Figures 6f and 6g). The shape of the pore pressure profiles versus distance from the slip surface is sharper than that for the temperature field, suggesting lower efficiency in fluid diffusion than heat transport. Our calculations further show that the pore pressure builds up mostly due to the TP effect (Figure 6h). Dehydration of smectite yields a pore pressure rise of ∼ 6 MPa, while fluid diffusion away from the slip zone is almost negligible (Figure 6h). In energy partitioning, reactions and heat diffusion only take up a negligible portion of the frictional work produced by the earthquake, and diffusion begins to become a significant effect to dictate the temperature evolution after the earthquake (Figure 6i).
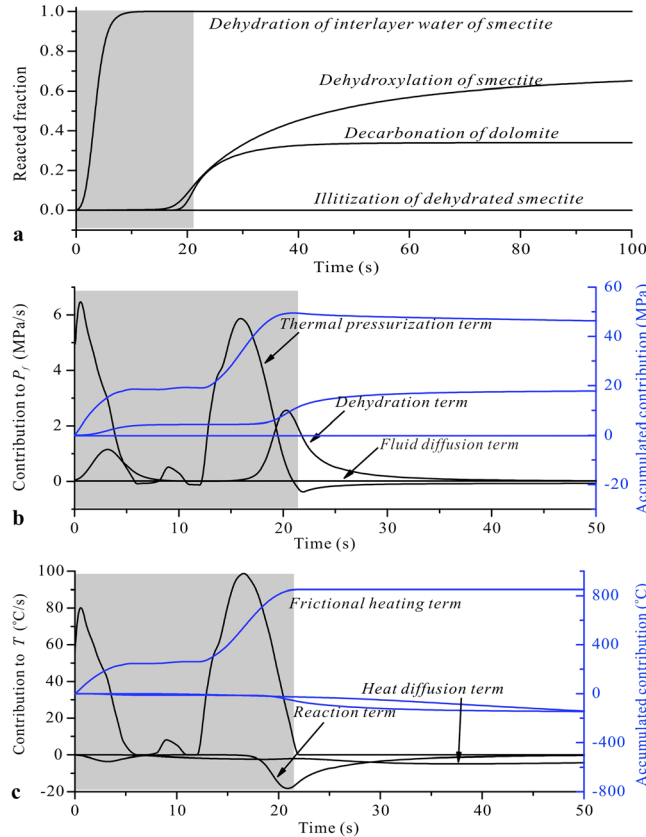
Figure 8. Modeling results of a case with extensive chemical reactions. (a) The evolution of reacted fraction of different reacting substances with time. The (b) pore pressure and (c) energy partitioning along with time. The results are from the case of Ref ‖ λ_0.1 ‖ CFP. The shaded areas denote the time span of the Wenchuan earthquake.

Figure 9. The computed *p-T* curves at the slip center in cases of slip localization.

5.4.2. Effects of Chemical Reactions

[43] In order to gain an insight of the potential effect of chemical reactions in the framework of a rapid slip event on a fault, we model the following cases: (1) the reference case without chemical reactions, (2) the reference case but without considering solid volume reduction due to reaction, and (3) the reference case without thermal pressurization. These cases are referred to as *Ref || no_react*, *Ref || ΔV_0*, and *Ref || no_TP*, respectively. The *p-T* curve of *Ref || no_react* is similar to that of the standard Ref case (Figure 7). If *ΔV_0* is assumed, the maximum temperature is reduced by 49°C in comparison with that reached in Ref. The *p-T* curve of *Ref || ΔV_0* exhibits a rapid increase in pore pressure at the very first stage of slip. Due to rapid reduction in effective normal stress, the fault becomes weaker, i.e., the shear stress is 3 MPa smaller than for Ref after the preslip. In the case of *Ref || no_TP*, excess pore pressure can only be generated by reactions. As shown in Figure 7, dehydration of smectite first causes a pore pressure rise of 6 MPa. As the temperature approaches ∼ 600°C, dolomite starts to decompose, resulting in a rapid buildup of pore pressure until it significantly exceeds the lithostatic pressure. The ultimate temperature rise is limited to sit below 897°C. This shows that in our study chemical reactions can limit temperature rise, not so much because they are endothermic but because of the release of fluid which causes reduction in effective normal stress.

[44] A chemical reaction can only occur to a significant extent after sufficient temperature rise causes adequate thermal activation of the reaction rate. To allow for extensive occurrence of reactions, we investigated the case *Ref || λ_0.1 || CFP*, where *CFP* signifies constant fluid properties. As discussed in section 6.3, low λ value and the use of CFP mean that more frictional heat can be produced. Here, in this case, a maximum temperature of 872°C is achieved (Figure 7). Despite full dehydration of smectite, dehydroxylation of smectite and decarbonation of dolomite occur to extents of 71% and 34%, respectively (Figure 8a). These chemical reactions cause a pore pressure rise of as much as 18 MPa, compared with 46 MPa by thermal pressurization (Figure 8b). In terms of energy partitioning, the energy taken up by these endothermic reactions is also comparable with that by diffusion (Figure 8c). As shown in Figure 7, the *p-T*

curves of *Ref || λ_0.1 || CFP* and *Ref || no_TP* are characterized by a distinct hysteresis signature, that is, the depressurization curves are well above the pressurization curves. We infer that this is caused by extra fluid mass released by chemical reactions. Since the reactions involved are all irreversible, they will not stop until the temperature falls below the threshold or all the reactants are consumed. This means that even though fluid pressurization becomes fully efficient so that no frictional heating can be produced anymore, the dewatering or degassing reactions will continuously provide fluid mass to the pore space, causing a prolonged increase of pore pressure. We emphasize that chemical reactions can help overshoot the normal stress acting on the fault plane and that such overshooting is impossible to occur in cases with TP only. That is because frictional heating will stop only if the pore pressure reaches the lithostatic pressure. In this sense, TP can only lead to pore pressure closely approaching the lithostatic pressure, but never exceeding it. Note that once overshoot occurs, the equation used for fluid flow cannot accurately describe the system any longer because of possible non-Darcy flow.
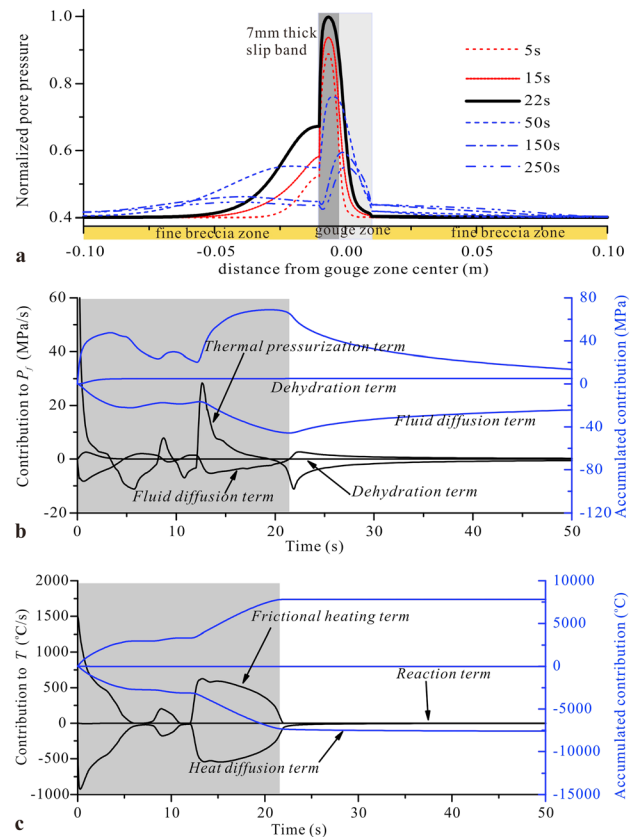
Figure 10. Modeling results of cases with slip localization. (a) Snapshots of the profile of normalized pore pressure across the fault core in the case of Ref || 7 mm thick slip band. (b) Pore pressure and (c) energy partitioning in the case of Ref || 0.5 mm thick slip band. The shaded area in Figure 10a represents the gouge zone and the dark part signifies the localized slip band. The shaded areas in Figures 10b and 10c denote the time span of the Wenchuan earthquake.
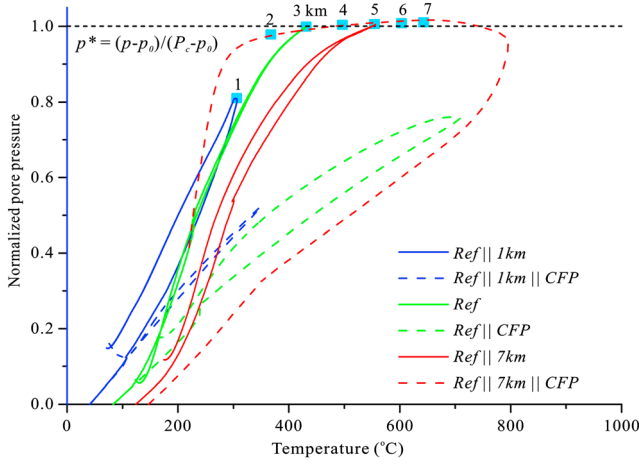
Figure 11. The computed p-T curves at the slip band center at various depths. Solid and dashed lines indicate the modeling results using SDFP and CFP, respectively. The blue squares denote the pore pressure and temperature conditions by the end of the slip event. For comparison purposes, the pore pressure is normalized by the initial pore pressure and lithostatic pressure as the formula labeled above.

5.4.3. Effect of Initial Pore Pressure

[45] The initial pore pressure inside the fault zone can vary greatly at depth. In order to test its influence on TP efficiency, we conducted modeling with λ values of 0.1, 0.2, 0.3, and 0.5 (referred to as $Ref \parallel \lambda\_0.1$, $Ref \parallel \lambda\_0.2$, $Ref \parallel \lambda\_0.3$, and $Ref \parallel \lambda\_0.5$). A larger temperature rise is expected for lower λ value because more energy is required to build up pore pressure to reach the overpressured condition under which frictional heating stops. However, the modeling results unexpectedly show that the p-T curves for various λ cases gradually converge as slip progresses (as marked in an ellipse in Figure 7). The maximum temperatures exhibit subtle increase from 425°C to 439°C when λ decreases from 0.5 to 0.1. We infer that this strongly relates to the introduction of SDFP. Actually when CFP is used, as shown in Figure 7, a prominent difference will be produced for various λ values (compare $Ref \parallel CFP$ and $Ref \parallel \lambda\_0.1 \parallel CFP$). Considering the limited contribution by diffusion and reaction (Figure 6h), the slope of the p-T curve can roughly represent the coefficient of thermal pressurization of the system (Λ), expressed as $(\alpha_f - \alpha_m)\Phi/S_s$. Because α_f tends to decrease with pressure in a low-temperature regime (Figure A1), higher TP efficiency should be expected for smaller λ values. As slip continues, the difference of pore pressure in various λ cases will get smaller and smaller until Λ become identical to each other.

5.4.4. Effect of Slip Band Thickness

[46] Field observations (Figure 2c) in combination with microscopic analysis on the natural and lab-sheared gouges suggested that coseismic slip might be localized (Figures 2c and 2e). Candidate values of the slip band thickness, W, are 20 mm if slip was distributed evenly in the entire gouge zone, ~7 mm if to represent the black gouge, and $W < 1$ mm to represent the microscale localization. Therefore, the effect of slip band thickness, ranging from 0.3 to 20 mm has been investigated (Figure 9). We let slip be localized at one margin of the gouge zone (Figure 10a) resembling the real fault

structure (Figures 2c and 2e), and the mesh grid was refined to make sure that more than 12 elements occupied the localized shear band. Due to the asymmetric distribution of transport properties relative to the shear band, the pore pressure exhibits asymmetric profiles (Figure 10a). The breccia zone directly in contact with the shear band has higher pore pressure compared with the other side. This is in agreement with a previous study investigating the influence of asymmetric permeability structure on fluid pressurization in response to frictional heating [*Vredevoogd et al.*, 2007]. In the case of a 7 mm thick slip band, the effect of "localization" is not conspicuous, producing a p-T curve similar to that of the Ref case. In contrast, the case of $Ref \parallel 0.5$ mm thick slip band exhibits much higher temperature and pore pressure increase, and the p-T curve thus differs strongly from that of the Ref case. Varying W (Figure 9) indicates that if the slip band is thicker than 2 mm, the maximum temperature achieved falls in a small range, i.e., from 431°C to 471°C. On the other hand, if W is smaller than 1 mm, the temperature rise is very sensitive to W (Figure 9). In other words, there exists a critical slip band thickness, W_{cr}, above and below which the TP shows contrasting behavior. This suggests that the variation in W can dramatically affect the overall efficiency of TP and hence lead to significant heterogeneity in the degree and rate of slip weakening along the fault plane.

[47] Theoretical studies suggest that TP efficiency depends strongly on the rate of propagation of the slip-induced fluid pressure pulse relative to the slip displacement [*Lachenbruch*, 1980; *Mase and Smith*, 1985]. The characteristic length of hydraulic diffusion during an earthquake L_f is $(t_s k/(\eta S_s))^{1/2}$, where t_s is the time span of an earthquake. According to our measurements, the gouge sample has a permeability of 1.0×10^{-21} m^2 and specific storage of 4.0×10^{-10} Pa^{-1} at 3 km depth. Substituting these values into the above formula gives an L_f of 0.66 mm. The W_{cr} value obtained (1–2 mm) is coincidently equal to ~ 2 times of L_f. If the shear band is thinner than W_{cr}, loss of pressurized fluid out from the heated zone can no longer be neglected. Temperature rise within the shear band is thus facilitated by more efficient fluid escape. As
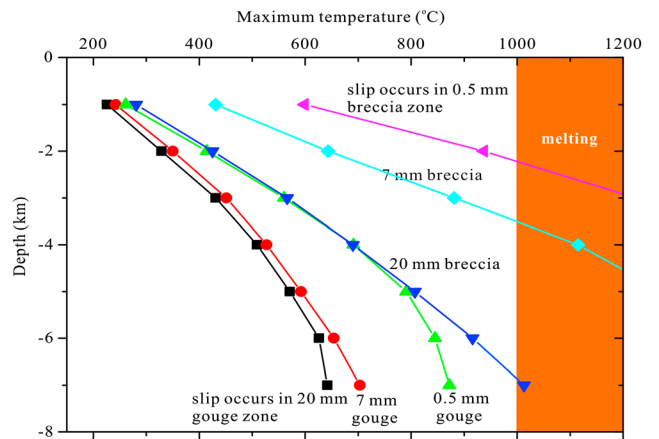
Figure 12. Comparison of the maximum temperature in cases when slip occurs in a gouge zone versus in the surrounding breccia zone. Suppose heating to 1000°C could cause local melting. The effect of slip band thicknesses (0.5, 7, and 20 mm) is also investigated.
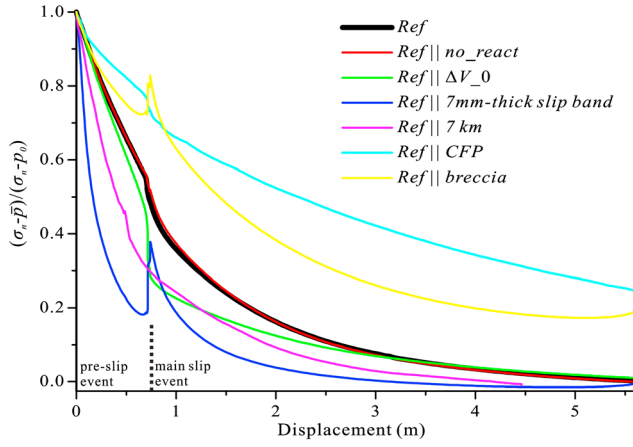
Figure 13. Evolution of normalized effective pressure along with displacement in various cases. Ref, reference case; Ref ‖ no_react, reference case without chemical reactions; Ref ‖ ΔV_0, reference case without considering solid volume reduction due to reaction; Ref ‖ 7 mm thick slip band, slip occurring in a localized shear band of 7 mm thick; Ref ‖ 7 km, slip occurring at 7 km depth; Ref ‖ CFP, reference case but using CFP; Ref ‖ breccia, slip branching into a surrounding breccia zone.

shown in Figure 10b, for a 0.5 mm thick shear band, the evolution of pore pressure is controlled by competition between TP and fluid diffusion outside the shear band (Figure 10b). Likewise, for the temperature field, heat transport almost balances frictional heating (Figure 10c). By contrast, if W is much larger than W_{cr}, the slip event can be taken as an "adiabatic and undrained" process [*Rice*, 2006]. In this case, the hydrothermal diffusion terms in equations (3) and (4) can be neglected, and evolution of temperature against pore pressure during a fault shearing can be then simplified as $\Delta T = \Lambda^{-1} \Delta p$, if assuming no chemical reactions [*Lachenbruch*, 1980; *Rice*, 2006]. Therefore, on a first-order approximation, the temperature rise is expected to be proportional to the potential increase of pore pressure, which is in agreement with the modeling results that the cases with W ranging from 2 to 20 mm show similar temperature rises (Figure 9).

5.4.5. Effect of Depth

[48] We also modeled coseismic TP processes at various depths (1–7 km). The fault gouge collected in the exposure studied is rich in smectite-rich I/S, which can survive dehydration to depths over 7 km, as evidenced by deep oil-well drillings [*Pollastro*, 1993]. The variation in the absolute content of smectite with depth was neglected here, but its effect on modeling results has been evaluated by varying the hydration state of smectite phase used in the modeling (see section 6.3). The slip history at depth is interpolated from the surface rupture offsets and the seismological inversion results (Figure 1e). At deep conditions, the increased normal stress implies that more frictional heat can be generated, while the fault rocks are expected to be more impermeable. Indeed, as shown in the Figure 11, calculation results indicate that the weakening effect is more efficient at depth. The maximum pore pressure attained is close to lithostatic pressure when the depth is greater than 2 km. Overshooting occurs at depths greater than 4 km. The

maximum temperature attained is facilitated by the larger increase in pore pressure possible at a greater depth, from 306° C at 1 km depth to 642°C at 7 km depth in our calculations. The contrast between results for various depths is much bigger when using CFP as discussed later in section 6.2.

5.4.6. Effect of Branching Slip

[49] Slip surfaces branching off the gouge zone and cutting into the surrounding breccia rocks are commonly observed on the outcrop scale, not only at the ZJG [*Yang et al.*, 2012] but also at other exposures [e.g., *Togo et al.*, 2011; *Hou et al.*, 2012] along the LFZ. To explore the effect of slip branching into the branches, we replaced the central gouge zone in our reference model with a fault breccia zone. The frictional and transport properties (Run 3 in Figure 5) of the coarse breccia were used.

[50] Figure 12 compares the temperature rise for slip in the gouge zone versus slip in the breccia zone. Much higher temperatures are achieved in the latter case, even causing extensive melting (1000°C is set as threshold for melting). To compare the effect of fluid pressurization on dynamic slip weakening, we plot the evolution of normalized effective pressure inside the slip band along with displacement (Figure 13), instead of shear resistance, to exclude the contribution from the evolution of μ_d. The results show that the reduction in effective pressure in the breccia zone is 20% less than that in the gouge zone (between Ref and *Ref ‖ breccia* in Figure 13). Because of rapid fluid escape, the result even displays transient recovery in the interval between the two
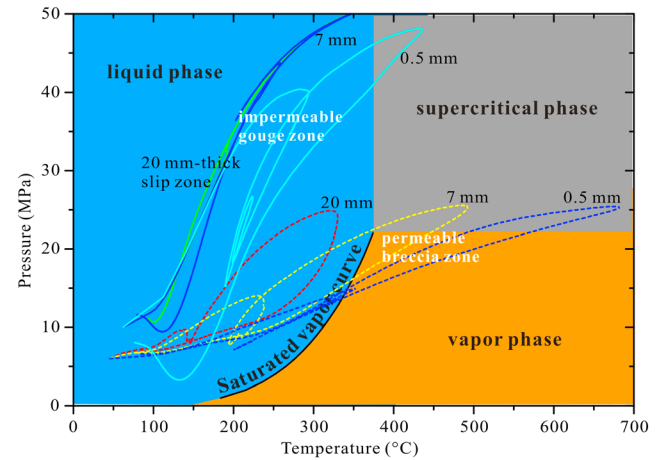
Figure 14. Comparison of *p-T* curves in cases when slip occurs in a gouge zone versus in a breccia zone. The calculations are at 2 km depth for slip in a gouge zone and at 1.2 km depth for slip in a breccia zone. In both cases, the initial pore pressure is set 0.2 of the lithostatic pressure. Note that since our modeling here does not consider phase changes of water, the portion of curves passing through the saturated vapor curve should be treated with caution because once the *p-T* state of pore water meets the saturated vapor curve, it will begin to vaporize. The considerable enthalpy change involved in this process can inhibit the temperature rise [*Brantut et al.*, 2011]. At the same time, vaporization strongly promotes pore pressure rise because water vapor has much lower density than liquid water. However, once vaporization occurs, the fluid flow enters the two-phase regime, which is beyond the capability of our finite element framework.

slip events (Figure 13). Moreover, the *p-T* curves exhibit much more gradual increase of pore pressure with temperature in comparison with the slip occurring in an impermeable gouge zone, implying a lower efficiency of TP (Figure 14). The comparative modeling results suggest that slip branching into the breccia zone can play an important role in determining the spatial distribution of pore pressure generation during an earthquake. Splaying of ruptures into surrounding breccia zones or into a permeable subsidiary fault will prevent excess pore pressure generation. Therefore, like variations in *W*, slip branching behavior may also cause heterogeneity of TP along the fault plane, thus influencing dynamic fault motion.

6. Discussion

[51] Our laboratory and numerical results have revealed several issues that require explanation and/or further analysis. They are as follows: (1) The transport properties of the fault rocks investigated show significant variability with effective pressure and with rock types. How can these data refine our understanding of the fluid flow pattern in the Wenchuan earthquake fault zone? (2) The dry and wet samples display distinctly different slip-weakening behavior at seismic slip rates. What does this discrepancy imply? (3) Our numerical modeling shows that the highly coupled thermal-hydrological-mechanical-chemical processes during fault motion are of great importance in influencing the coseismic slip-weakening behavior. What is the sensitivity of this weakening to the various controlling factors? How did these processes influence coseismic rupturing on the Wenchuan earthquake fault?

6.1. Hydrological Architecture of the Fault Zone

[52] The discussion here is based on our transport property data obtained for samples taken across the fault zone, as measured in the upward pressurization path. As shown by the results of these measurements (Figure 5), the central gray gouge and microfractured limestone at the margin of the fault zone have the lowest permeability. They are below $2 \times 10^{-18} \, m^2$ at a P_e higher than 20 MPa. By contrast, the fault breccias surrounding the gouge zone have much higher permeability, greater than $5 \times 10^{-19} \, m^2$ at the P_e value investigated. The cemented breccia and microfractured limestone near the fault margin show the lowest porosity and specific storage values (Figure 5b). They decrease to unmeasurable levels in the intact country rock. The gouge sample studied also has relatively low porosity, especially at a P_e value above 30 MPa. Therefore, the transport properties across the fault zone at the ZJG exposure take on a typical "conduit/barrier" binary structure as proposed by *Caine et al.* [1996]. This is in agreement with a previous study performed using nitrogen as fluid medium under low-pressure conditions [*Chen et al.*, 2011] and also with the permeability structure revealed in other active fault zones [*Mizoguchi et al.*, 2008; *Tanikawa et al.*, 2009]. The implication is that the fault fluid is mainly stored in the porous damaged zone, and its flow is constrained between the barriers of fault gouge and country rock. Thus, the hydrological architecture of the LFZ shows strong a macro-anisotropy; thereby, fluid flow is easy in the direction parallel to the fault plane.

[53] The variations in transport properties across the fault are presumably related to the contrast in structural and material properties of the fault rocks, e.g., load-supporting framework, grain size distribution, and clay content. The microfractured limestone has very low porosity, and its permeability and specific storage are extremely sensitive to effective pressure (Figure 5). This can be explained by the crack-dominated structure. The gouge sample, consisting of very fine grains with an average diameter of 4 μm and containing a large percentage of clay minerals, has a typical matrix-supported structure and low porosity (Figure 2d), which could strongly reduce the fluid transport efficiency with increasing effective pressure [*Bernabé et al.*, 2004]. In contrast, the fault breccias show a clast-supported framework structure which is relatively resistant to compaction, thus exhibiting less sensitivity to effective pressure (Figure 5).

[54] As a final note on the hydrological architecture of the fault zone, it is expected that low permeability is required in and around the fault zone in order to maintain the high P_f needed to nucleate a high-angle thrust rupture [*Sibson et al.*, 1988; *Zhou and He*, 2009] at a midcrustal depth [*Zhang et al.*, 2010]. At that depth, the low-friction minerals found at the surface (e.g., smectite, I/S) are unlikely to exist and hence are unlikely to have played a dominant role over p_f in determining rupture behavior at depth. However, our lab measurements showed quite high permeability for the coarse fault breccias of the damaged zone. We believe this can be explained by the following reasons: (1) The fault rocks investigated have undergone severe fault motion and damage during the Wenchuan earthquake. They were sampled ~ 11 months after the Wenchuan earthquake, hence more likely reflecting the hydrological architecture of the fault zone in the postseismic stage. (2) Fluid-involved mechanisms such as precipitation, cementation, and pressure solution can help heal the fault rocks at depth in a long term. Just like the cemented breccia zone on the hanging wall of the exposure studied, the samples in this zone are composed of fine matrix and scattered fragments, whereas they are well cemented and rare macrofracture can be seen in it (strictly, this kind of rock should be termed cataclasite). We infer that their formation has recorded deformation inherited from past fault motion, presumably by repeated earthquakes and by fluid-assisted healing in long-term interseismic periods. However, these are out of the reach of this study.

6.2. Thermal Pressurization in the High-Velocity Experiments

[55] The friction behavior for water-dampened samples is characterized by rapid slip weakening and by lower steady state frictional strength (Figure 4d) than the dry samples (Figure 4c). For the fault gouge, in particular, the dynamic weakening process is completed in the very first stage of slip (Figure 4b). This can be explained as pressurization of pore water by frictional heating provided both the gouge material and the sealing capacity of the Teflon sleeve contribute to restricting fluid flow. Similar weakening behavior has been reported for natural fault gouge [*Ujiie et al.*, 2011], landslide surface gouge [*Ferri et al.*, 2010], and simulated gouge samples [*Faulkner et al.*, 2011] and was explained as a TP process in these studies also. Conspicuous dilation, observed in our wet experiments, supports this viewpoint. Moreover, much smaller d_c values have been obtained in our wet experiments (0.6–2.0 m, Figure 4d) than in our dry experiments (2–35 m, Figure 4c). This implies an extra slip-weakening mechanism associated with the
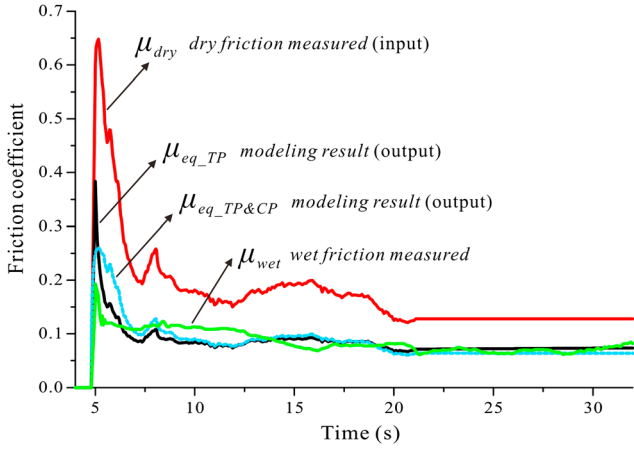
Figure 15. Comparison of the measured dry and wet friction data versus equivalent frictional strength derived from modeling. In the modeling, the dry friction data (μ_{dry}, red line) was imported to specify the heat source, and the calculated equivalent friction (μ_{eq}) was compared with wet friction observed (μ_{wet}, green line). μ_{eq_TP} (dark line) corresponds to the case that TP is considered, while $\mu_{eq\_TP\&CP}$ (blue line) corresponds to the case that both TP and initial compaction (initial pore pressure was assumed to increase by 0.2 MPa) have been taken into account. Note that the dry friction data only lasted 23 s and have been extrapolated to 32.7 s, assuming constant friction after 23 s.

presence of water. The lack of a systematic relationship between d_c and the applied normal stress under wet conditions can be explained by fluid pressurization of the pore water, which leaked in an unreproducible manner, from run to run due to the poor sealing capacity of the Teflon sleeves.

[56] To test whether TP can explain the dramatically different frictional behavior observed between wet and dry experiments, a finite element (FE) model for simulating the high-velocity experiments was constructed. The FE approach is the same as that used for fault slip modeling but employed 2-D axisymmetric geometry and appropriately rewritten partial differential equations. Initial and boundary conditions, as well as detailed parametric settings of the model are addressed in detail in Appendix B. The dry friction data (Figure 4b) were imported to specify the heat source, given as $Q_{so} = \tau \dot{\gamma} = 2\pi \varpi r \mu_{dry}(\sigma_n - \overline{p}(r))/W$. Here ϖ is the rotation rate (s^{-1}), r is the distance from the rotation axis, μ_{dry} is the dry friction, σ_n is the normal stress imposed, and W is the gouge layer thickness. The friction between the rotary wall rock and Teflon sleeve is an additional heat source, which can be calculated from the Teflon friction correction data (Figure 4a). Unlike our planar fault model, the vertically averaged pore pressure ($\overline{p}$) is a function of r ($\overline{p}(r) = \int_{-W/2}^{W/2} p(r,z)dz/W$). The calculated result is then compared with the measured wet friction data. If TP is the only mechanism responsible for weakening in the wet experiments, the calculated equivalent friction (μ_{eq}), defined as

$$\mu_{eq} = \frac{\int_0^R \mu_{dry}(\sigma_n - \overline{p}(r))2\pi r^2 dr}{\int_0^R \sigma_n 2\pi r^2 dr} \quad (10)$$

should be identical to that observed in the wet experiment.

Here, μ_{wet} is the measured wet friction and R is the radius of the host gabbro cylinder. The modeling results (Figure 15) show that the equivalent friction (marked by μ_{eq_TP}) agrees well with the measured wet friction (marked by μ_{wet}), in particular at steady state. The slip-weakening distance is reduced from 4.0 m in the dry case to less than 2.0 m. However, for the first few seconds, μ_{eq_TP} peaks to a value well above μ_{wet} and is followed by a much dramatic slip weakening than that seen in the wet experiment. The most obvious explanation for this discrepancy is initial compaction by grain comminution at the onset of slip. The axial shortening observed at the onset of slip supports this viewpoint. To examine this further, the initial pore pressure was assumed to increase by an amount of 0.1–0.2 MPa due to initial compaction. An increase of 0.2 MPa was sufficient to decrease the equivalent peak friction by ~ 0.15 ($\mu_{eq\_TP\&CP}$ in Figure 15), bringing the overall trend of the equivalent friction close to the measured wet friction curve. A second possible explanation is the change in sealing capacity of the Teflon sleeve. In the simulations, water is allowed to permeate freely through the interface between the Teflon sleeve and the host gabbro. This is what happens when the Teflon sleeve has expanded after running for a few seconds. However, at the onset of slip, the Teflon sleeve could have partially sealed the pore pressure, causing an initial spike in pore pressure in the initial stage of motion.

[57] Under dry conditions, even though dehydration of smectite releases some water, our dry model shows that the effect of pressurization of free fluid by frictional heating can be neglected. Detailed settings of the model for the dry case are given in Appendix B. The results show that vaporization of water lost from the smectite occurs at the very beginning of slip (0.2 s after slip) and that ~ 2/3 of the outer radius of the gouge layer reaches the critical temperature for vaporization during the dry run. In spite of this, the pore pressure rises by less than 0.1 MPa (1/10 of σ_n) due to high compressibility and easy escape of the low-viscosity pore gases. The weakening effect caused by vaporization of dehydrated water is thus small. As a first approximation, our dry friction data can therefore be used to calculate the heat source in modeling coseismic slip at depth. The dynamic stress drop observed can then be explained by flash heating [*Goldsby and Tullis*, 2011], even though thermal decomposition of the carbonate minerals present [*Han et al.*, 2007] cannot be fully ruled out (Table 1). The conclusion drawn from our high-velocity experiments is that TP is an important process in thin layers of wet fault gouge at coseismic slip rates and exerts a strong control on the magnitude of slip weakening and on d_c.

6.3. Role of Coseismic Thermochemical Processes and Implications for the Wenchuan Earthquake

[58] Our numerical analyses, which incorporated the measured physical and chemical properties of the local fault rocks, are believed to provide a realistic way of modeling the main features of the faulting process of the 2008 Wenchuan earthquake. The results indicate that TP should have occurred extensively at depth and effectively reduced the dynamic shear resistance during the Wenchuan earthquake. The most crucial parameter determining dynamic rupture propagation, acceleration, and the energy partitioning inside the fault zone during earthquakes [*Ida*, 1972; *Marone*

et al., 2009] is the effective slip-weakening distance (defined as the critical distance over which shear resistance drops to the residual level), denoted as D_c. This should be carefully distinguished from the laboratory-derived d_c (Figure 4f) which only reflects the weakening caused by the evolution of friction. According to the extrapolation of our experiment results, d_c at 3 km depth (at a P_e of 45 MPa) is ~ 0.036 m (Table 2), which is much lower than the seismologically inferred value of 0.52 m for the Wenchuan earthquake [*Liu and Shi*, 2011]. However, TP can first raise d_c to a moderate level of 0.22 m on the basis of the empirical equation obtained describing the relation between d_c with normal stress (Figure 4f), and then raises it further to the seismological level (~ 0.5) through reducing the effective normal stress acting on the fault plane.

[59] Taken together with previous work, our study demonstrates that chemical reactions, in particular smectite dehydration, may have played an important role in rupture propagation during the Wenchuan earthquake. First, dehydration of smectite is predicted to start at the onset of slip, and the reaction rate is very fast (Figure 6). Second, at the ZJG exposure, there is evidence that illitization induced by frictional heating occurred in the thin black gouge during the Wenchuan earthquake [*Chen et al.*, 2013]. Third, a growing number of studies on surface exposures [*Dang et al.*, 2012; *Hou et al.*, 2012; *Zhang et al.*, 2013; *Chen et al.*, 2013; *Yao et al.*, 2013] and drilling cores [*Xu and Li*, 2010] have revealed that the enrichment in smectite (or smectite-rich I/S) is a common feature for the Longmenshan fault zone. Although pure smectite is unstable at depths beyond 2–3 km [*Saffer and Marone*, 2003], I/S can survive to depths over 7 km, as evidenced by deep oil-well drilling [*Pollastro*, 1993]. Smectite dehydration is therefore expected to have occurred extensively along the Wenchuan earthquake fault up to such depths.

[60] The dynamic effect of smectite dehydration on faulting depends on the content and hydration state of the smectite in the gouge sample. These will both vary with increasing depth (c.f. data from San Andreas Fault Observatory at Depth presented by *Solum et al.* [2006] and *Lockner et al.* [2011]), but no quantitative constraints are available. The variation of smectite content with depth is not taken into account in our modeling. However, its effect on modeling results has been evaluated by varying the hydration state of the smectite content (10.7 wt %) measured in the gray gouge (χ in equation 7 and Table 3). In our modeling, 10.7 wt. % smectite with one interlayer H_2O generates about 6 MPa excess pore pressure (Figures 6, 8, and 11). This value increases to 16.5 MPa if three interlayers of water molecules are initially present in the smectite. We consider this to be the maximum effect of smectite dehydration because both smectite content and hydration state are expected to decrease with depth. Competing effects (i.e., reaction enthalpy change and solid volume shrinkage) associated with reactions act to affect generation of excess pore pressure as well. For reactions involving clay alteration, the endothermic effect is negligible relative to frictional heating (Figure 6i). With high reaction enthalpy, decarbonation can potentially function as an important buffer of temperature rise (Table 3; Figures 7 and 8). However, high temperature (> 600°C) is required to activate this reaction, and in our modeling, it only occurs in cases of highly localized slip (Figure 9) or branching slip

or at very deep condition (Figure 12). Dehydroxylation of smectite starts at ~ 400°C. Since the reaction rate is slow (Table 3), its contribution to the coseismic process is limited, though it would occur continuously during the postseismic stage. The reaction of smectite-to-illite transformation is the slowest of reactions involved. Its effect in terms of fluid pressurization is negligible in all our analyses even when high temperature is achieved. Moreover, volume change in the solid phases has to be taken into consideration; otherwise, an overestimation of fluid pressurization will result (Figures 7 and 13).

[61] The reaction-enhanced TP process would have increased the pore pressure inside the slip zone thereby moderating the temperature rise during the Wenchuan earthquake. Heat generation is facilitated by more efficient fluid escape from the heated zone, either associated with localized (Figure 9) or branching slip (Figure 12), or to a lesser extent, with the large pore pressure rise possible at depth (Figure 11). Typically as in the exposure studied, principal slip gouges in active fault zones usually contain abundant clay minerals [e.g., *Lockner et al.*, 2011] and have very fine grain size [e.g., *Ma et al.*, 2006]. Statistical analysis (23 in total) has indicated that fault gouges found in almost all active fault zones have permeability lower than 10^{-18} m^2 [*Chen and Yang*, 2012]. These factors tend to inhibit the temperature rise through enhanced fluid pressurization by potential dewatering reactions [*Yamaguchi et al.*, 2011] and by reducing fluid transportation [*Bernabé et al.*, 2004]. Therefore, the now widely accepted concept of TP offers a compelling explanation for the apparent scarcity of pseudotachylite in natural faults [*Sibson*, 1975; *Rice*, 2006; *Sibson and Toy*, 2006]. If the hydrous mineral present in a fault zone is abundant enough, melting is unlikely to occur easily since dehydration reactions, occurring at the very start of slip, will effectively slow down heat production [*Brantut et al.*, 2011]. Our results thus agree favorably with the assertion that pseudotachylite can only be produced in dry, crystalline rocks, as reported by *Sibson and Toy* [2006].

[62] Coseismic pressurization of pore fluid is a complex process involving interplay between frictional heating, reaction, and diffusion. According to systematic parametric analysis (i.e., λ, W, and depth; with/without reactions; branching slip), our results show that W and permeability (branching slip) are the most important factors influencing TP efficiency (Figure 13), as proposed in previous studies [e.g., *Rice*, 2006; *Sulem and Famin*, 2009]. The influence of depth can be attributed mostly to permeability change as well. If a slip zone propagates into a localized band or branches to an adjacent breccia zone or immature splay (Figure 13), it will lead to enhancement of fluid escape, partially inhibiting TP as a slip-weakening mechanism. This suggests that branching or localized slip can lead to a pronounced heterogeneity in fluid pressure distribution along the fault, which could result in variations in the degree and rate of slip weakening, hence influencing the dynamics of fault motion [*Wibberley and Shimamoto*, 2005]. Although it is difficult to incorporate along-strike variations in properties (i.e., W and k) of the slip zones into modeling work on the gross slip response, we infer that rupture propagation will be locally controlled by these slip-resistant points. In other words, fault branches and localized slip locations may act as seismic asperities. This mechanism can also help explain

why the almost complete dynamic strength drop seen in our simulations (e.g., Figure 6) is not reflected as a stress drop in natural earthquakes [*Zhang et al.*, 2009].

[63] The coseismic rupture was associated with the largest fault offsets near the exposure studied (Figure 1c). Friction experiments at seismic slip rates revealed relatively low friction for the gouge sample (Figure 4). However, there is not much difference from the gouges sampled from other segments along the LFZ, e.g., the Pingxi exposure at the northeast terminus [*Yao et al.*, 2013], the Hongkou exposure close to the epicenter [*Togo et al.*, 2011], or the Chaping exposure in the central segment [*Hou et al.*, 2012]. The acceleration of slip from depth upward (Figure 1d) suggests that the coseismic motion was not passively pushed from depth, and there must be an extra mechanism allowing acceleration. We propose that fluid pressurization within the fluid-saturated fault zone may have been responsible for this. First, as stated above, our friction experiments on wet gouge samples and numerical analysis indicate that the reaction-enhanced TP would have occurred easily at the ZJG exposure, and the modeling results are in broad agreement with seismological observations. Second, previous modeling work [*Mizoguchi and Shimamoto*, 2008] has demonstrated that TP is an important slip-weakening mechanism when the permeability of fault gouge is lower than $10^{-18}\,\mathrm{m}^2$. Third, the efficiency of TP that occurred near the ZJG exposure is expected to be higher than elsewhere along the LFZ. This is because the gouge sample of the ZJG exposure shows so far the lowest permeability ($7.3 \times 10^{-22}\,\mathrm{m}^2$ at a P_e of 165 MPa) in comparison with four other gouges along the LFZ. They are 2.6×10^{-20}, 4.3×10^{-20}, 1.7×10^{-19}, and $9.2 \times 10^{-19}\,\mathrm{m}^2$ for Pingxi, Jinghe, Hongkou, and Shenxigou exposures, respectively (see their locations in Figure 1c). Recall that TP is dependent not only upon the permeability of the slip zone, but also upon other factors such as slip band thickness. To exclude the influence of other factors, thorough experimental and modeling work needs to be done on other locations. On the basis of our findings, we propose a new approach to seismic hazard assessment in the future, whereby TP efficiency should be incorporated. Such an approach cannot predict the spatiotemporal distribution of the nucleation site but can provide an evaluation of the response of a fault (or segment) to the earthquake rupture if an earthquake has already nucleated. Though accuracy cannot be declaimed and possibility for validation of our model is elusive, our work does provide a basic method for evaluating TP efficiency.

[64] Further, our modeling work shows that the local PT conditions inside the slip zone can vary through a large range during faulting, so the pore fluid may even undergo multiple phase changes, from the liquid to supercritical states as well as existing in the gaseous form (Figure 14). Accordingly, the fluid properties can vary by up to 2 orders of magnitude (Figure A1). There are indeed several competing factors associated with evolving fluid properties that influence TP efficiency. It is therefore difficult to say whether the introduction of SDFP facilitates TP or not. We conducted modeling with SDFP and CFP separately (Figures 7 and 11) to evaluate the potential impact of fluid properties on TP efficiency. Basically, in the cases of SDFP, the pore pressure can build up more rapidly than for the cases of CFP. The temperature increases, though, when assuming that CFP are much larger

than assuming SDFP (Figures 7 and 12). The results indicate that the variation of fluid properties during faulting has played a crucial role that can strongly influence slip processes and likely did strongly affect the evolution of the Wenchuan earthquake, much more so than previously realized.

7. Conclusions

[65] The coseismic slip associated with the Wenchuan earthquake has been systematically investigated based on the combined experimental and modeling work and considering the effects of a range of thermal-hydrological-mechanical-chemical processes within the slip zone. Main conclusions are summarized below.

[66] 1. High-velocity friction experiments revealed low steady state friction for both fault breccia and central fault gouge samples collected from the exposure studied. The wet results are characterized by rapid slip weakening and by lower friction than the dry results, suggesting the presence of friction-induced fluid pressurization in thin layers of wet gouges.

[67] 2. The gouge samples show the lowest permeability and low porosity compared with the fault rocks from the surrounding damaged zone, such as coarse fault breccias. The intact country rocks also have low permeability, even below the detection of our experimental configuration. The hydrological profile across the fault zone thus exhibits a typical conduit/barrier binary structure, with fluid flow being constrained to occur in the highly damaged zone on each side of the central gouge.

[68] 3. Numerical modeling of coseismic slip using the measured fault rock properties and seismological data on slip rate and displacement indicated that thermochemical pressurization played an important role during the Wenchuan earthquake, with dynamic stress reduction being strongly enhanced by increase of pore pressure due to frictional heating and with calculated slip-weakening distance being consistent with the seismologically inferred level. Overshooting of lithostatic pressure by pore pressure generation might have occurred at depth, limiting temperature development to values less than 600°C. There was more than enough heat generated to fully dehydrate the interlayer water in smectite, which can contribute an excess pore pressure of ~ 6 MPa. Fluid pressurization within the slip zone can help explain the large coseismic displacement and slip acceleration observed near Beichuan city. We propose that TP should be considered in future seismic hazard assessment.

[69] 4. Slip wedging into a localized fault or splaying into a surrounding breccia zone will lead to enhanced fluid loss, partially inhibiting the TP process. We speculate that the locations where localized or branching slip occurs will behave as strong portion of the fault that may act as seismic asperities. There exists a critical thickness, W_{cr}, which is approximately equal to 2 times the characteristic hydrological diffusion length. If the coseismic slip band is thicker than W_{cr}, major TP weakening is possible.

[70] 5. State-dependent fluid thermophysical properties are newly introduced in this work. Their use shows fluid pressurization to be much more efficient than when these properties are taken as constant and equal to the values for a reference state. The changes in temperature and pressure conditions that occur in the fault core during fault motion allow the pore
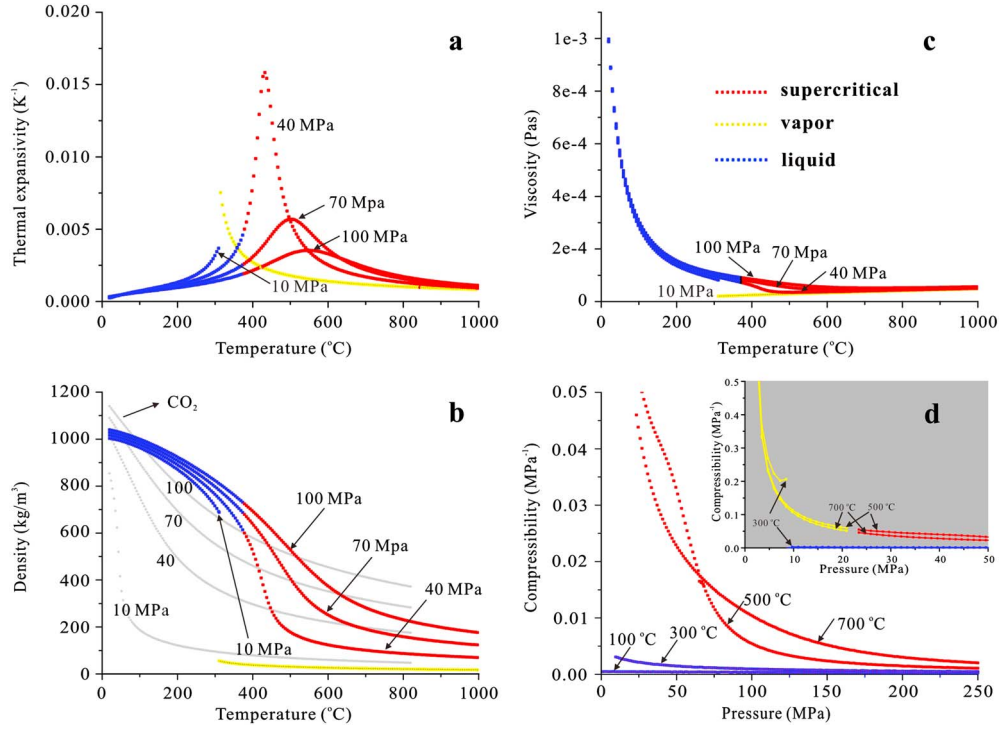
Figure A1. State-dependent thermodynamical properties of pure water, including (a) thermal expansivity, (b) density, and (c) dynamic viscosity as functions of temperature, as well as (d) compressibility as a function of pressure. The insert plot in Figure A1d is the enlarged graph for the low pressure part. Density of pure CO_2 is also presented in Figure A1b.

fluid to undergo multiple phase changes. The corresponding changes in fluid properties may play a determining role in earthquake dynamics and are much more important than previously realized.

Appendix A: The State-Dependent Thermophysical Properties of Water

[71] Within the PT range of our modeling, the fluid properties, i.e., thermal expansivity, density, viscosity, and compressibility, can vary significantly (Figure A1). In an attempt to model the situation more realistically, we employ state-dependent fluid properties, with pure water as a proxy for the natural pore fluid. To avoid data singularity at the phase boundaries, the p-T graph is divided into three domains on basis of the three-phase diagram (Figure 14): Domain I—supercritical phase: $p \geq 22.06$ MPa and $T \geq 373.9°C$, Domain II—liquid phase: $T < 373.9°C$ and above the saturated vapor curve, and Domain III—vapor phase: $p < 22.06$ MPa and below the saturated vapor curve. The database of thermophysical properties of water downloaded from the National Institute of Standards and Technology (NIST, http://webbook.nist.gov/chemistry/fluid/) is then fitted employing a five-order polynomial. It is expressed as $Y(T, p) = \sum_{i=0}^{4} \sum_{j=0}^{4} A_{ij} T^i p^j$, where T is the temperature in unit of °C, p is the pore pressure in MPa, Y is the dependent variable such as density, and A_{ij} is the corresponding coefficient matrix.

Appendix B: Model Settings for Simulating the High-Velocity Experiments

[72] A FE model was constructed for simulating high-velocity experiments under both dry and wet conditions. Model geometry, meshing, boundary conditions, and detailed settings for key parameters were as follows:

[73] 1. The sample assembly (Figure 3a) was represented using a 2-D axisymmetric FE geometry, consisting of the gouge sample, the wall-rock cylinders, the Teflon sleeve, the sample grips, and the loading shaft. The geometrical model was meshed self-adaptively using triangular elements (5531 in total).

[74] 2. Gouge friction was the main heat source (Figure 4b). Friction between the rotary wall rock and Teflon sleeve is an additional heat source, calculated from the Teflon friction correction data (Figure 4a). The boundaries of the loading frame were assumed to be at a fixed temperature of 20°C, and the temperature of surfaces exposed to air was assumed to evolve following Newton's cooling law. The thermal conductivities of the gouge and gabbro host rock were measured using a TK04 thermal conductivity meter (TeKa, Germany). Specific heat capacities of the wall rock and gouge sample were calculated from specific heat of the constituent minerals and their mass fraction.

[75] 3. Permeability, porosity, and specific storage values for the gouge sample were based on extrapolations from our experimental data (Figure 5), neglecting damage induced by preparation and shear of the gouge. The wall rock (Indian gabbro) is practically impermeable ($\sim 1 \times 10^{-22}$ m^2). The sealing capacity of the Teflon ring is assumed to be

negligible. The initial pore pressure was set at atmospheric, unless otherwise stated.

[76] 4. The composition of the fault gouge was based on our XRD data (Table 1).

[77] 5. The properties for pore gases (in dry experiments) were assumed to be represented by data for nitrogen, as obtained from the NIST website. The liquid-vapor phase transition was also considered, as this can promote pore pressure increase and inhibit temperature rise. For the dry experiments, we assumed that once the temperature reaches the critical temperature for vaporization, the smectite interlayer water will be released as water vapor. The enthalpy change associated with the phase transition is simulated by increasing the enthalpy of the reaction by an appropriate amount. The contribution of water vapor to the pore pressure generation rate was calculated from equation (7), using the density of water vapor as download from NIST. When modeling the wet experiments, vaporization is ignored as a first approximation (because the resultant two-phase flow is beyond the capability of the present FE framework), yielding a minimum TP effect.

References

Bayer, G. (1973), Thermal expansion anisotropy of oxide compounds, *Proc. Br. Ceram. Soc.*, *22*, 39–53.

Bernabé, Y., U. Mok, B. Evans, and F. J. Herrmann (2004), Permeability and storativity of binary mixtures of high- and low-permeability materials, *J. Geophys. Res.*, *109*, B12207, doi:10.1029/2004JB003111.

Bernabé, Y., U. Mok, and B. Evans (2006), A note on the oscillating flow method for measuring rock permeability, *Int. J. Rock Mech. Min. Sci.*, *43*, 311–316.

Birch, F. (1966), Compressibility: Elastic constants, in *Handbook of Physical Constants*, edited by D. P. Clark, Jr., *Geol. Soc. Amer. Mem.*, 97, pp. 97–174.

Bizzarri, A., and M. Cocco (2006), A thermal pressurization model for the spontaneous dynamic rupture propagation on a three-dimensional fault: 1. Methodological approach, *J. Geophys. Res.*, *111*, B05303, doi:10.1029/2005JB003862.

Brace, W. F., J. B. Walsh, and W. T. Frangos (1968), Permeability of granite under high pressure, *J. Geophys. Res.*, *73*, 2225–2236.

Brantut, N., A. Schubnel, J.-N. Rouzaud, F. Brunet, and T. Shimamoto (2008), High-velocity frictional properties of a clay-bearing fault gouge and implications for earthquake mechanics, *J. Geophys. Res.*, *113*, B10401, doi:10.1029/2007JB005551.

Brantut, N., A. Schubnel, J. Corvisier, and J. Sarout (2010), Thermochemical pressurization of faults during coseismic slip, *J. Geophys. Res.*, *115*, B05314, doi:10.1029/2009JB006533.

Brantut, N., R. Han, T. Shimamoto, N. Findling, and A. Schubnel (2011), Fast slip with inhibited temperature rise due to mineral dehydration: Evidence from experiments on gypsum, *Geology*, *39*(1), 59–62.

Bray, H. J., and S. A. T. Redfern (1999), Kinetics of dehydration of Ca-montmorillonite, *Phys. Chem. Miner.*, *26*, 591–600, doi:10.1007/s002690050223.

Caine, J. S., J. P. Evans, and C. B. Forster (1996), Fault zone architecture and permeability structure, *Geology*, *24*, 1025–1028.

Chen, J., and X. Yang (2012), The permeability of earthquake fault, *Earth Sci. Front.*, *19*(4), 30–40. (in Chinese with English abstract)

Chen, J., X. Yang, J. Dang, C. He, Y. Zhou, and S. Ma (2011), Internal structure and permeability of Wenchuan earthquake fault, *Chinese J. of Geophys*, *54*(7), 1805–1916. (in Chinese with an English abstract)

Chen, J., X. Yang, S. Ma, and C. J. Spiers (2013), Mass removal and clay mineral de/re-hydration in carbonate-rich portions of the Wenchuan earthquake fault: Geochemical evidence and implications for fault zone evolution and coseismic slip, *J. Geophys. Res. Solid Earth*, *118*, doi:10.1002/jgrb.50089.

Criado, J. M., M. Gonzalez, J. Malek, and A. Ortega (1995), The effect of the CO_2 pressure on the thermal decomposition kinetics of calcium carbonate, *Thermochim. Acta*, *254*, 121–127.

Dang, J., Y. Zhou, L. Hang, C. He, J. Chen, X. Dang, and X. Yang (2012), Fault gouge in carbon mudstone at outcrops of Bajiaomiao and Shenxigou in Hongkou, *Seismology and Geology*, *34*(1), 17–27. (in Chinese with English abstract)

David, C., T.-f. Wong, W. Zhu, and J. Zhang (1994), Laboratory measurement of compaction- induced permeability change in porous rocks: Implications for the generation and maintenance of pore pressure excess in the crust, *Pure Appl. Geophys.*, *143*, 425–456.

de Lorenzo, S., and M. Lpddo (2010), Effect of frictional heating and thermal advection on pre-seismic sliding: A numerical simulation using a rate-, state- and temperature-dependent friction law, *J. Geodyn.*, *49*(1), 1–13.

De paola, N., T. Hirose, and T. Mitchell (2011), Fault lubrication and earthquake propagation in thermally unstable rocks, *Geology*, *39*(1), 35–38.

Di Toro, G., D. Goldsby, and T. E. Tullis (2004), Friction falls towards zero in quartz rock as slip velocity approaches seismic rates, *Nature*, *427*, 436–439.

Di Toro, G., R. Han, T. Hirose, N. De Paola, S. Nielsen, K. Mizoguchi, F. Ferri, M. Cocco, and T. Shimamoto (2011), Fault lubrication during earthquakes, *Nature*, *471*, 493–499.

Famin, V., S. Nakashima, A.-M. Boullier, K. Fujimoto, and T. Hirono (2008), Earthquakes produce carbon dioxide in crustal faults, *Earth Planet. Sci. Lett.*, *265*(3–4), 487–497.

Faulkner, D. R., and E. H. Rutter (2000), Comparison of water and argon permeability in natural clay-bearing fault gouge under high pressure at 20°C, *J. Geophys. Res.*, *105*, 16,415–16,427.

Faulkner, D. R., T. M. Mitchell, J. Behnen, T. Hirose, and T. Shimamoto (2011), Stuck in the mud? Earthquake nucleation and propagation through accretionary forearcs, *Geophys. Res. Lett.*, *38*, L18303, doi:10.1029/2011GL048552.

Ferri, F., G. Di Toro, T. Hirose, and T. Shimamoto (2010), Evidence of thermal pressurization in high-velocity friction experiments on smectite-rich gouges, *Terra Nova*, *22*(5), 347–353.

Fine, R. A., and F. J. Millero (1973), Compressibility of water as a function of temperature and pressure, *J. Chem. Phys.*, *59*(10), 5529–5536, doi:10.1063/1.1679903.

Fischer, G. J., and M. S. Paterson (1992), Measurement of permeability and storage capacity in rocks during deformation at high temperature and pressure, in *Fault Mechanics and Transport Properties of Rocks*, edited by B. Evans, and T.-F. Wong, pp. 187–211, Academic Press, New York.

Goldsby, D. L., and T. E. Tullis (2011), Flash heating leads to low frictional strength of crustal rocks at earthquake slip rates, *Science*, *334*, 216–218.

Hamada, Y., T. Hirono, W. Tanikawa, W. Soh, and S.-R. Song (2009), Energy taken up by co-seismic chemical reactions during a large earthquake: An example from the 1999 Taiwan Chi-Chi earthquake, *Geophys. Res. Lett.*, *36*, L06301, doi:10.1029/2008GL036772.

Han, R., T. Shimamoto, T. Hirose, J. Ree, and J. Ando (2007), Ultralow friction of carbonate faults caused by thermal decomposition, *Science*, *316*, 878–881.

Han, R., T. Hirose, and T. Shimamoto (2010), Strong velocity weakening and powder lubrication of simulated carbonate faults at seismic slip rates, *J. Geophys. Res.*, *115*, B03412, doi:10.1029/2008JB006136.

Hirono, T., et al. (2006), Evidence of frictional melting from disk-shaped black material, discovered within the Taiwan Chelungpu fault system, *Geophys. Res. Lett.*, *33*, L19311, doi:10.1029/2006GL027329.

Hirono, T., et al. (2008), Clay mineral reactions caused by frictional heating during an earthquake: An example from the Taiwan Chelungpu fault, *Geophys. Res. Lett.*, *35*, L16303, doi:10.1029/2008GL034476.

Hirose, T., and M. Bystricky (2007), Extreme dynamic weakening of faults during dehydration by coseismic shear heating, *Geophys. Res. Lett.*, *34*, L14311, doi:10.1029/2007GL030049.

Hirose, T., and T. Shimamoto (2005), Growth of molten zone as a mechanism of slip weakening of simulated faults in gabbro during frictional melting, *J. Geophys. Res.*, *110*, B05202, doi:10.1029/2004JB003207.

Hou, L., S. Ma, T. Shimamoto, J. Chen, L. Yao, X. Song, and Y. Okimura (2012), Internal structures and high-velocity frictional properties of a bedding-parallel carbonate fault at Xiaojiaqiao outcrop activated by the 2008 Wenchuan earthquake, *Earthquake Sciences*, *25*, 197–217.

Hu, J., Z. Duan, C. Zhu, and I.-M. Chou (2007), PVTx properties of the CO_2-H_2O and CO_2-H_2O-NaCl systems below 647 K: Assessment of experimental data and thermodynamic models, *Chem. Geol.*, *238*(3–4), 249–267.

Huang, W. L., J. M. Longo, and D. R. Pevear (1993), An experimentally derived kinetic model for smectite-to-illite conversion and its use as a geothermometer, *Clays and Clay Minerals*, *41*, 162–177.

Huang, W. L., W. A. Bassett, and T. C. Wu (1994), Dehydration and hydration of montmorillonite at elevated temperatures and pressures monitored using synchrotron radiation, *Am. Mineral.*, *79*, 683–691.

Ida, Y. (1972), Cohesive force across the tip of a longitudinal-shear crack and Griffith's specific surface energy, *J. Geophys. Res.*, *77*, 3796–3805.

Ikehara, M., et al. (2007), Low total and inorganic carbon contents within the Chelungpu fault, *Geochem. J.*, *41*, 391–396.

Kanamori, H. (1994), Mechanics of earthquakes, *Ann. Rev. Earth Planet. Sci.*, *22*, 207–237.

Ko, S.-C., D. L. Olgaard, and T.-F. Wong (1997), Generation and mainte-nance of pore pressure excess in a dehydrating system, 1 Experimental and microstructural observations, *J. Geophys. Res.*, *102*, 825–839.

Kranz, R. L., J. S. Saltzman, and J. D. Blacic (1990), Hydraulic diffusivity measurements on laboratory rock samples using an oscillating pore pressure method, *Int. J. Rock Mech. Min. Sci.*, *27*, 345–352.

Lachenbruch, A. H. (1980), Frictional heating, fluid pressure, and the resistance to fault motion, *J. Geophys. Res.*, *85*(B11), 6097–6112.

Lin, X., F. Ying, and N. Zheng (1992), Techniques of X-ray Diffraction Analysis and Its Geological Application, pp. 119–131, Petroleum Industry Press, Beijing. (in Chinese with an English abstract)

Liu, B. Y., and B. P. Shi (2011), The state of stress of the M_s 8.0 Wenchuan earthquake faulting and its implication to the aftershock hazard, *Chinese J. Geophys.*, *54*(4), 1002–1009. (in Chinese with English abstract)

Lockner, D. A., C. Morrow, D. Moore, and S. Hickman (2011), Low strength of deep San Andreas fault gouge from SAFOD core, *Nature*, *472*, 82–85.

Ma, K.-F., et al. (2006), Slip zone and energetics of a large earthquake from the Taiwan Chelungpu-fault Drilling Project, *Nature*, *444*, 473–476.

Marone, C., M. Cocco, E. Richardson, and E. Tinti (2009), The critical slip distance for seismic and aseismic fault zones of finite width, in *Fault-Zone Properties and Earthquake Rupture Dynamics*, International Geophysics Series, vol. 94, edited by E. Fukuyama, pp. 135–162, Elsevier, New York.

Mase, C., and L. Smith (1985), Pore-fluid pressure and frictional heating on a fault surface, *Pageoph, Pure Appl. Geophys.*, *122*, 583–607.

Mizoguchi, K., and T. Shimamoto (2008), A combined thermal pressuriza-tion and high-velocity behavior Nojima fault gouge to infer slip-weakening of a fault. *AOGS annual meeting*, Abstract, 58-SE-A1507.

Mizoguchi, K., T. Hirose, T. Shimamoto, and E. Fukuyama (2007), Reconstruction of seismic faulting by high-velocity friction experiments: An example of the 1995 Kobe earthquake, *Geophys. Res. Lett.*, *34*, L01308, doi:10.1029/2006GL027931.

Mizoguchi, K., T. Hirose, T. Shimamoto, and E. Fukuyama (2008), Internal structure and permeability of the Nojima fault, southwest Japan, *J. Struct. Geol.*, *30*, 513–524.

Mori, J. J. (2010), Temperature Measurements in the WFSD-1 Borehole Following the 2008 Wenchuan Earthquake, *American Geophysical Union*, *fall annual meeting*, San Francisco, T53E-03.

Noda, H., and T. Shimamoto (2005), Thermal pressurization and slip weakening distance of a fault: An example of the Hanaore fault, southwest Japan, *Bull. Seismol. Soc. Am.*, *95*(4), 1224–1233, doi:10.1785/0120040089.

Noyan, H., M. O¨nal, and Y. Sarikaya (2008), Thermal deformation thermo-dynamics of a smectite mineral, *J. Therm. Anal. Calorim.*, *91*, 299–303, doi:10.1007/s10973-007-8260-z.

Ohnaka, M., and L.-F. Shen (1999), Scaling of the rupture process from nucleation to dynamic propagation: Implications of geometric irregularity of the rupturing surfaces, *J. Geophys. Res.*, *104*, 817–844.

Pollastro, R. M. (1993), Considerations and applications of the illite/smectite geothermometer in hydrocarbon-bearing rocks of Miocene to Mississippian age, *Clay and Clay minerals*, *4*(2), 119–133.

Reches, Z., and D. A. Lockner (2010), Fault weakening and earthquake instability by power lubrication, *Nature*, *467*, 452–455.

Rice, J. R. (1999), Flash heating at asperity contacts and rate-dependent friction, *Eos. Trans. AGU*, *80*(46), Fall Meet. Suppl., F681.

Rice, J. R. (2006), Heating and weakening of faults during earthquake slip, *J. Geophys. Res.*, *111*, B05311, doi:10.1029/2005JB004006.

Sabirzyanov, A. N., R. A. Shagiakhmetov, F. R. Gabitov, A. A. Tarzimanov, and F. M. Gumerov (2003), Water solubility of carbon dioxide under supercritical and subcritical conditions, *Theor. Found. Chem. Eng.*, *37*(1), 51–53, doi:10.1023/A:1022256927236.

Saffer, D. M., and C. Marone (2003), Comparison of smectite- and illite-rich gouge frictional properties: Application to the updip limit of the seismogenic zone along subduction megathrusts, *Earth Planet. Sci. Lett.*, *215*, 219–235.

Samuelson, J., D. Elsworth, and C. Marone, (2009), Shear-induced dilatancy of fluid-saturated faults: Experiment and theory, *J. Geophys. Res.*, *114*, B12404, doi:10.1029/2008JB006273.

Sawai, M., T. Shimamoto, and T. Togo (2012), Reduction in BET surface area of Nojima fault gouge with seismic slip and its implication for the fracture energy of earthquakes, *J. Struct. Geol.*, *38*, 117–138.

Segall, P., and J. R. Rice (2006), Does shear heating of pore fluid contribute to earthquake nucleation?, *J. Geophys. Res.*, *111*, B09316, doi:10.1029/2005JB004129.

Shi, Y., and C. Y. Wang (1986), Pore pressure generation in sedimentary basins: Overloading versus aquathermal, *J. Geophys. Res.*, *91*(B2), 2153–2162.

Sibson, R. H. (1975), Generation of pseudotachylyte by ancient seismic faulting, *Geophys. J. Int.*, *43*(3), 775.

Sibson, R. H. (1977), Fault rocks and fault mechanisms, *J. Geol. Soc.*, *133*, 191–213.

Sibson, R. H., and V. Toy (2006), The habitat of fault-generated pseudotachylyte: Presence vs. absence of friction-melt, in *Radiated Energy and the Physics of Faulting*, *Geophysical Monograph Series*, edited by R. Abercrombie, et al., vol. 170, pp. 153–166, AGU, Washington, D. C.

Sibson, R. H., F. Robert, and H. Poulsen (1988), High-angle reverse faults, fluid-pressure cycling and mesothermal gold-quartz deposits, *Geology*, *16*, 551–555.

Smith, S. A. F., A. Billi, G. Di Toro, and R. Spiess (2011), Principal slip zones in limestone: Microstructural characterization and implications for the seismic cycle (Tre Monti fault, central Apennines, Italy), *Pure Appl. Geophys.*, *168*, 2365–2393.

Solum, J. G., S. H. Hickman, D. A. Lockner, D. E. Moore, B. A. van der Pluijm, A. M. Schleicher, and J. P. Evans (2006), Mineralogical characterization of protolith and fault rocks from the SAFOD Main Hole, *Geophys. Res. Lett.*, *33*, L21314, doi:10.1029/2006GL027285.

Sulem, J., and V. Famin (2009), Thermal decomposition of carbonates in fault zones: Slip-weakening and temperature limiting effects, *J. Geophys. Res.*, *114*, B03309, doi:10.1029/2008JB006004.

Sulem, J., P. Lazar, and I. Vardoulakis (2007), Thermo-poro-mechanical properties of clayey gouge and application to rapid fault shearing, *Int. J. Numer. Anal. Meth. Geomech.*, *31*, 523–540.

Tanaka, H., W. M. Chen, C. Y. Wang, K. F. Ma, N. Urata, J. Mori, and M. Ando (2006), Frictional heat from faulting of the 1999 Chi-Chi, Taiwan earthquake, *Geophys. Res. Lett.*, *33*, L16316, doi:10.1029/2006GL026673.

Tanikawa, W., M. Sakaguchi, T. Hirono, W. Lin, W. Soh, and S.-R. Song (2009), Transport properties and dynamic processes in a fault zone from samples recovered from TCDP Hole B of the Taiwan Chelungpu Fault Drilling Project, *Geochem. Geophys. Geosyst.*, *10*, Q04013, doi:10.1029/2008GC002269.

Tanikawa, W., H. Mukoyoshi, O. Tadai, T. Hirose, A. Tsutsumi, and W. Lin (2012), Velocity dependence of shear-induced permeability associated with frictional behavior in fault zones of the Nankai subduction zone, *J. Geophys. Res.*, *117*, B05405, doi:10.1029/2011JB008956.

Togo, T., T. Shimamoto, S. Ma, and T. Hirose (2011), High-velocity fric-tional behavior of Longmenshan fault gouge from Hongkou outcrop and its implications for dynamic weakening of fault during 2008 Wenchuan earthquake, *Earthquake Science*, *24*, 267–281.

Tsutsumi, A., and T. Shimamoto (1997), High-velocity frictional properties of gabbro, *Geophys. Res. Lett.*, *24*(6), 699–702.

Ujiie, K., A. Tsutsumi, and J. Kameda (2011), Reproduction of thermal pressurization and fluidization of clay-rich fault gouges by high-velocity friction experiments and implications for seismic slip in natural faults, in *Geology of the Earthquake Source: A Volume in Honor of Rick Sibson*, edited by A. Fagereng, et al., vol. 359, pp. 267–285, Geological Society, London.

Vredevoogd, M. A., D. D. Oglesby, and S. K. Park (2007), Fluid pressuriza-tion due to frictional heating on a fault at a permeability contrast, *Geophys. Res. Lett.*, *34*, L18304, doi:10.1029/2007GL030754.

Vrolijk, P., and B. van der Pluijm (1999), Clay gouge, *J. Struc. Geol.*, *21*, 1039–1048.

Wibberley, C. A. J. (2002), Hydraulic diffusivity of fault gouge zones and implications for thermal pressurization during seismic slip, *Earth Planets Space*, *54*, 1153–1171.

Wibberley, C. A. J., and T. Shimamoto (2005), Earthquake slip weakening and asperities explained by thermal pressurization, *Nature*, *436*, 689–692.

Wong, T.-F., S.-C. Ko, and D. L. Olgaard (1997), Generation and maintenance of pore pressure excess in a dehydrating system 2. Theoretical analysis, *J. Geophys. Res.*, *102*(B1), 841–852.

Xu, X., X. Wen, G. Yu, G. Chen, Y. Klinger, J. Hubbard, and J. Shaw (2009), Coseismic reverse- and oblique-slip surface faulting generated by the 2008 M_w 7.9, Wenchuan earthquake, China, *Geology*, *37*(6), 515–518.

Xu, Z., and H. Li (2010), New Results from the Wenchuan Earthquake Fault Scientific Drilling Project (WFSD), *American Geophysical Union*, *fall annual meeting*, San Francisco, Abstract T53E-01.

Yamaguchi, A., et al. (2011), Progressive illitization in fault gouge caused by seismic slip propagation along a megasplay fault in the Nankai Tough, *Geology*, *39*(11), 995–998.

Yang, T., J. Chen, H. Wang, and H. Jin (2012), Rock magnetic properties of fault rocks from the rupture of the 2008 Wenchuan earthquake, China and their implications: Preliminary results from the Zhaojiagou outcrop, Beichuan County (Sichuan), *Tectonophysics*, *530*, 331–341.

Yao, L., S. Ma, T. Shimamoto, and T. Togo (2013), Structures and highvelocity frictional properties of the Pingxi fault zone in the Longmenshan fault system, Sichuan, China, activated during the 2008 Wenchuan earthquake, *Tectonophysics*, *599*, 135–156.

Zhang, L., and C. He (2013), Frictional properties of natural gouges from Longmenshan fault zone ruptured during the Wenchuan Mw7.9 earthquake, *Tectonophysics*, *594*, 149–164.

Zhang, P., X. Wen, Z. Shen, and J. Chen (2010), Oblique, high-angle, listric-reverse faulting and associated development of strain: The Wenchuan earthquake of May 12, 2008, Sichuan, China, *Annu. Rev. Earth Planet. Sci.*, *38*, 353–382.

Zhang, Y., W. Feng, L. Xu, C. Zhou, and Y. Chen (2009), Spatio-temporal rupture process of the 2008 great Wenchuan earthquake, *Science in China* (Series D: Earth Sciences), *52*(2), 145–154.

Zhou, X. (1993), Hydrogeochemical characteristics and formation of subsurface brines of deep aquifers in Longnu temple brine-bearing structure, Sichuan Basin, *Geoscience*, *7*(1), 83–92. (in Chinese with English abstract)

Zhou, Y., and C. He (2009), The rheological structures of crust and mechanics of high-angle reverse fault slip for Wenchuan Ms 8.0 earthquake, *Chinese J. Geophys.*, *52*(2), 474–484. (in Chinese with English abstract).